universität
wien

DIPLOMARBEIT

Titel der Diplomarbeit

„A table-top demonstration of radiation pressure"

Verfasserin

Dilek Demir

angestrebter akademischer Grad

Magistra der Naturwissenschaften (Mag. rer.nat)

Wien, 2011

Studienkennzahl lt. Studienblatt:	A 0600046
Studienrichtung lt. Studienblatt:	A411 Diplomstudium Physik
Betreuerin / Betreuer:	Univ.-Prof. Dr. Markus Aspelmeyer

A table-top demonstration of radiation pressure

Dilek DEMIR

Universität Wien

Fakultät für Physik

October 9, 2011

Abstract

The observation of the momentum transfer of light, the so-called radiation pressure, goes back to the seminal experiments by Lebedew and by Nichols and Hull in 1901. Up to now, all experimental demonstrations of this effect with macroscopic mirrors relied on a well-shielded experimental environment and were operated in vacuum and at high light powers.

This work describes a simple table-top experiment that illustrates the momentum transfer between light and a suspended mechanical mirror both under ambient conditions and in a low - pressure environment.

Our work is enabled by the development of millimeter-sized cantilevers of high reflectivity ($> 99.99\%$), very low spring constant ($\approx 0.031 \pm 0.003$ N/m to 0.0009 ± 0.0001 N/m) and very low levels of optical absorption (< 100 ppm).

Using these devices in an optical lever arrangement we demonstrate radiation pressure effects while operating in air, at room temperature and with only modest (< 10 mW) laser power. The behaviour of the cantilevers at low pressures is used to validate the nature of the radiation - pressure effect.

Zusammenfassung

Die Beobachtung, dass Licht Strahlungsdruck ausüben kann, geht zurück auf die bahnbrechenden Experimente von Lebedew, Nichols und Hull im Jahr 1901.

Ein einfaches Experiment zeigt, dass die Dynamik zwischen Licht und einem mikro-mechanischen Spiegel auf Umgebungstemperatur im Vakuum demonstriert werden kann.

Unsere Arbeit wird durch die Entwicklung von millimetergroßen mechanischen Hebeln ermöglicht. Diese sind hochreflektierend ($> 99,99\%$), haben eine sehr niedrige Federkonstante ($0,031 \pm 0,003 N/m - 0,0009 \pm 0,0001 N/m$) und sehr niedrige optische Absorption ($< 100 ppm$).

Mit Hilfe dieser Geräte in einer optische Hebelanordnung ist uns der Nachweis des Strahlungsdrucks bei Raumtemperatur an der Luft und bei niedriger Laserleistung ($< 10 mW$) gelungen. Zudem wird auch die Positionsänderung der mechanischen Hebel aufgrund des Strahlungsdrucks bei niedrigerem Druck überprüft.

Contents

List of Figures

List of Tables

Chapter 1

Introduction

The concept of radiation pressure (mathematically described in 2.3.1) is known since the early 16th century [27], when philosophers started thinking about the fact that light can exert a pressure which moves material. Around 1900 renown scientists like Fresnel, Bartoli, Boltzmann, Einstein, Euler, DeMarian, DuFay, Benette, Homberg, Zöllner, Fitzgerald, Goldhammer and others were searching for the evidence of this effect experimentally and theoretically.
Today, the radiation pressure force is fundamental in the new emerging field of quantum optomechanics that aims at achieving coherent quantum control of massive mechanical objects. It is in the heart of experiments such as feedback - cooling of mechanical motion (see [12]), strong coupling of opto - mechanics (e.g.[14]), cavity cooling of the mechanical resonator (e.g.[24]), parametric amplification of the mechanical motion [25] and levitation of nanometer sized objects [13], [2], [3], [4], [64],[5] and [6].

A lot of experiments are profiting from the use of radiation pressure but there are also applications where precision is needed. In this experiment radiation pressure is limiting the highly sensitive measurements with increasing power. This noise limit is known as the Standard Quantum Limit (SQL)[11], [10], [8], [7].

Some of the main developments in radiation pressure research were:
1619 Kepler suggested that the tails of comets exist due to the solar radiation that vaporizes particles on the surface of the comets [1].
1687 Newton was a strong proponent of the corpuscular theory. He calculated radiation pressure and supported the idea of the pressure due to sunlight. Euler was a devotee of the conception that light is a wave and he also confirmed the idea of radiation pressure. The question which property light has separated the scientists, but the pressure due to light was accepted from both.

1986 Arthur Ashkin manipulated microparticles with the radiation pressure force of laser light [13].
1901 Lebedew [26], Nichols and Hull [27] experimentally verified the theory using elegant torsion balance experiments.
1933 O. Frisch, Experimenteller Nachweis des Einsteinschen Strahlungsrückstoßes [28]. In this experiment a stream of sodium - atoms was illuminated with resonant light. The steering deflection of the atoms due to the momentum transfer during the absorption and emission was detected.
1936 R.A.Beth, Mechanical detection of the angular momentum of light [29].
1997 Chu, Cohen - Tannoudij and Philips win the Nobel Prize in Physics for cooling and trapping atoms in which they applied the radiation pressure force.

In the following we want to demonstrate the radiation pressure effect on a macroscopic object in a new parameter regime. 111 years ago (see [26], [27]) this effect was visible at pressures around $1 \cdot 10^{-5} mbar$ with $100mg$ metallic vanes. These were driven with optical powers of $\approx 0.5W$. Whereas, we observed the radiation pressure effect under ambient condition at room temperature. We operate at low optical powers in the rang of $\approx mW$ and with micro - mirrors which have an effective mass of $0.6\mu g$ (see 3).

1.1   Bartoli, Einstein and the Radiation Pressure Effect

The question whether light exerts a pressure or not was not answered in the 17th or 18th century. The corpuscular emission theory of light was taken to imply the existence of light pressure. The wave theory was regarded as incompatible with such a pressure.

    In 1865 Maxwell [18] dealt theoretically with the problem of light pressure from an entirely different perspective.
He applied the new electromagnetic theory [18] of light   "....in a medium in which waves are propagated there is a pressure in the direction normal to the waves .... rays falling on a thin metallic disk, delicately suspended in a vacuum, might perhaps produce an observable mechanical effect." He adds:" ......however, the electromagnetic light pressure was very small and quite insufficient to account for the radiometer or similar experiments."

Maxwell´s radiation pressure was not assigned a high status and had very little immediate impact.
1898, Lord Rayleigh admitted that the argument by which Maxwell originally deduced the pressure of radiation [is] "... not clear to me." He preferred the derivation given by J.J. Thompson [19].

Renewed interest arose when Crookes [27] constructed his light mill (or radiometer) in 1874 -75. He suggested that the revolution of the vanes of the mill was a direct result of the mechanical energy of light (radiant heat).

1874 Bartoli, who was primarily an experimental physicist, discussed radiation pressure independent of any particular theory. He derived the concepts of radiation pressure from thermodynamical considerations. Whereas Maxwell´s results are based on the electromagnetic wave theory of light.

Bartoli´s work is frequently cited as a source of inspiration for Boltzmann in his establishment of the Stefan-Boltzmann law of black body radiation. 1874 Bartoli discussed radiation pressure independent of any particular theory of light. Based on thought experiments (see 1.1.1) he concluded that radiation possibly exerts a pressure. He tested the hypothesis experimentally at first unaware of Crook´s work.
The experiments performed by Bartoli in 1874-75 were essentially of the same type as those of Crookes but Bartoli examined light light balances rather than light mills.
For the experiment he used balances in evacuated glass sphere such as a balance with a metal plate fastened at one end. To test the impact of light a strong beam of sunlight was focused on the plate at angles varying between 30 and 40 degrees. With this set-up Bartoli was not able to detect any motion which could describe the impact of light. The conclusion of Bartoli´s first experimental test was if such a pressure exists, it must be very small.

A student of Bartoli was Einstein in 1895 in Pavia, Italy. Einstein was influenced by the work of Bartoli, especially from the radiation pressure concept. This concept was the basic for the photoelectric effect [22] and the energy-mass-equivalence.
He talked at the 81st meeting of the *"Society of Natural Scientists and Medics"* in Salzburg, 1909. The title of his talk *" Über die Entwicklung unserer Anschauung über das Wesen und die Konstitution der Strahlung"*. Einstein´s question was: "Assuming Plank´s formula for black body radiation spectrum is correct: What can be deduced about the constitution of radiation?" In order to answer the question the Gedankenexperiment is presented in subsection 1.1.2.

1.1.1 Bartoli´s Gedankenexperiment: The Cycle

From [15],[16]. The walls of the cylinder are permeable and perfectly reflecting. A and D are fixed black bodies. B and C are reflecting pistons. Let the temperature of D be larger than that of A in situation 1. In 2, the piston B is removed transversely and the piston C pushed downwards towards D, leaving the cavity AC in thermal equilibrium with A.
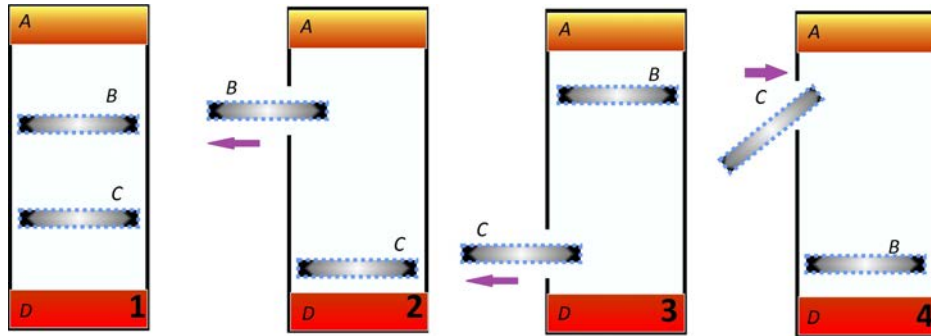
Figure 1.1: This picture shows the Bartoli´s cycle.

In 3, B is reset and C removed from its bottom position. In 4, B is pushed downwards and C put into the original position of B. The net result is a transfer of heat from A to D.

After some arguments his final result, relating the radiation pressure to the heat energy per unit area and the velocity

$$p = \frac{2Q}{v}E \qquad (1.1)$$

where E is the mechanical equivalent of heat, Q is the power received by one area and v is the velocity of radiant heat.

The Gedankenexperiment originally consists of spherical shells but Bartoli replaced the spherical shells with a cylinder and two moving pistons to make it more realistic.

He introduced radiation pressure to explain the situation of the spherical reflector C around the black sphere D. Step 3 in the picture above.

The more the volume of the enclosure with radiation energy is decreased to zero, the higher the chance that energy is transferred to D.

Each surface element is subjected to a repulsive pressure due to the heat radiation emitted by the black body D in the center of the shall, independent of any change of the surface.

Looking at the infinitesimal change in internal radiation energy with the work done to perform an infinitesimal change of the radius

$$p\delta R = \frac{2Q}{v}E\delta R \qquad (1.2)$$

where p describes the pressure due to radiation, Q is the power received by one area unit of C. The relation for the radiation pressure to the heat energy per unit area and velocity is

$$p = \frac{2Q}{v}E \qquad (1.3)$$

1884 Boltzmann pointed out that the first equation is valid in the special case of heat radiation falling upon the black body.

For the derivation of equation 1.2 Bartoil believed that he made use of the second law of thermodynamics.

If the vibration of internal energy with a temperature T is taken into account, then the first law of thermodynamics should be used.

Boltzmann and later Galitzine [20] generated the theory without changing the main results. The pressure due to heat is direct proportional to the energy and inverse proportional to the velocity of radiation, which is in agreement with Maxwell´s result.

According to Bartoli´s derivation the heat radiant is independent of any particular theory of light. In his experiments Bartoli could never measure the pressure due to light successful. His conclusion was that there is no light pressure. He came to that final remark because of his own failure to detect light pressure as well as his theoretical argument that light pressure cannot cause Crook´s radiometer to revolve. He determines that there is no light pressure. After his death, in 1903, the Accademia dei Lincei published a sealed memoir[1]. His final argumentation was that *radiation can not produce any pressure* but then some other mechanism had to be found to reconcile the thought experiment with the second law (see [15]).

Bartoli gave new ideas for making this effect visible. One is a metallic surface moving perpendicular with respect to the direction of impinging radiation. Then the surface will experience a resistance opposite to the direction of the motion.

1.1.2   Einstein´s Gedankenexperiment: The Box

At that time the Plank´s formula for blackbody radition spectrum was known. The fundamental formula for the energy density at a frequency ν is

$$\rho = \frac{8\pi h\nu^3}{c^3} \frac{1}{e^{\frac{h\nu}{kT}} - 1} \tag{1.4}$$

where k is the Boltzmann Constant, T the temperature bath and h the Plank constant.

His defence to the question about the consitution of radiation was the following "Gedankenexperiment":

Consider a perfectly reflecting, harmonically bound mirror in a box within on the left and right side of the mirror is a perfect reflector and the temperature T is the same. Besides the closed box is not reflecting or scattering anything from outside to the inside.

A motion is possible when the mean kinetic energy is equal to the third

---

[1]this was already submitted in 1882
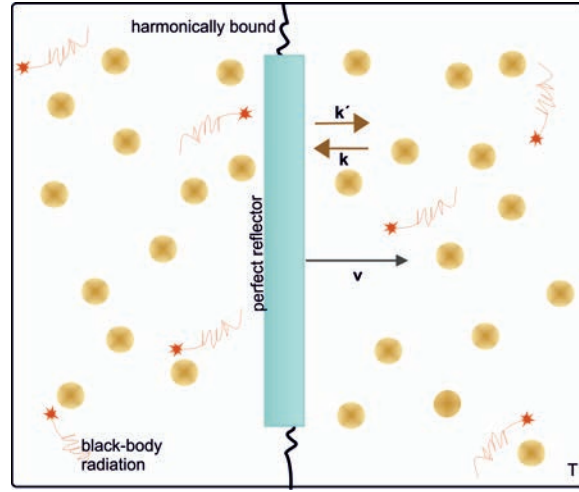
Figure 1.2: This picture shows Einstein´s box.

mean kinetic energy of a monoatomic gas molecule, which is a consequence of statistical mechanics.

If a wave is reflected from the mirrors front face, than the photons are seeing a Doppler-Shift

$$\bar{k} = -k\left(1 - \frac{2v}{c}\right) \tag{1.5}$$

The radiation pressure force due to the momentum transfer $\approx k - \bar{k}$ on the mirror is

$$F_{RadiationPressure} = -\frac{2P}{c}\left(1 - \frac{v}{c}\right) \tag{1.6}$$

where P is the power. According to Einstein this provides a friction

$$\dot{p} = -\gamma p \tag{1.7}$$

where

$$\gamma = \frac{2P}{mc^2} \tag{1.8}$$

which is similar to the "Doppler cooling" of a mirror.
The open question is : Is the system in thermal equilibrium?
According to Plank´s formula the radiation pressure force is fluctuating and this causes a momentum diffusion of the mirror. The averaged squared momentum transferred, due to radiation pressure fluctuations, is

$$\bar{\Delta}^2 = \frac{1}{c}\left(h\rho\nu + \frac{c^3}{8\pi}\frac{\rho^2}{\nu^2}\right)d\nu f\tau \tag{1.9}$$

The first term describes a localized particle moving with the energy $h\nu$ and the second term describes an interference effect.

Einstein´s conclusion is radiation has both, particle and wave characteristic.

Organization of the Thesis

We will first look at the theory of micro - mechanical oscillators (chapter 2) in order to understand the basics of the system under study. The third chapter (see 3) will focus on the highly reflective mirrors. All this will be followed by the experimental result (chapter 4). Here we explain why we believe that radiation pressure dominates our system and understand the measurements, for the final radiation pressure demonstration. Finally (chapter 5) we want to point out that this system is extendable and beneficial not only for the radiation pressure demonstration.

Chapter 2

Theory

In this chapter we will focus on the mechanics of the tested cantilevers. In order to understand the system´s behaviour, we need to understand the behaviour of undamped, damped and forced oscillators. In order to accomplish this we had to solve (non-) linear differential equations.
Secondly the reader will be introduced into the optics, which we needed for the demonstration. This section is essential for understanding the properties of the underlying optical elements. Additionally we answer questions concerning the experimental design.
Finally, we will discuss the fundamental radiation pressure formula.

2.1 Mechanics

This section and the following ones are discussed in most textbooks such as [33, 35, 36, 37].

2.1.1 Undamped Oscillator

Consider a solid with mass m fixed at the end of a spring. At the zero position ($x = 0$) the mass will always have a total force equal to zero as Gravity and the force produced by the spring, which are acting on the system at every point, are cancelling each other. The more the mass is displaced from the zero position the more the spring´s force will increase.
Hooke´s Law describes the restoring force, which pushes m back to $x = 0$

$$\vec{F} = -kx\vec{e_x} \tag{2.1}$$

where $\vec{e_x}$ is the unit vector in x-direction and x the mass position at any time and k represents the spring constant, which depends on the material properties and geometry of the spring material as well as the thickness of the spring.

The resulting equation of motion is

$$- kx = m\frac{d^2x}{dt^2} \tag{2.2}$$

Using the relation $\omega_0^2 = \frac{k}{m}$ equation 2.2 can be written as

$$\frac{d^2x}{dt^2} + \omega_0^2 x = 0 \tag{2.3}$$

This describes an undamped harmonic oscillator. One solution for equation 2.2 is

$$x = c \exp(\lambda t) \tag{2.4}$$

where c is an arbitrary complex constant. We can now use 2.4 in 2.3 to obtain the equation

$$\lambda^2 + \omega_0^2 = 0 \tag{2.5}$$

for the parameter λ we find

$$\lambda_1 = +i\omega_0^2 \tag{2.6}$$

$$\lambda_2 = -i\omega_0^2 \tag{2.7}$$

Or

$$x_1 = c_1 \exp(+i\omega_0 t) \tag{2.8}$$

$$x_2 = c_2 \exp(-i\omega_0 t) \tag{2.9}$$

These solutions are linearly independent for $\omega_0 \neq 0$. From the theory of differential equations we know that the general solution of this linear and homogeneous differential equation is a linear combination of both solutions, and hence we have

$$x(t) = c_1 \exp(+i\omega_0 t) + c_2^* \exp(-i\omega_0 t) \tag{2.10}$$

The constants can be determined from the boundary conditions of the individual oscillation problem.

2.1.2 Damped Oscillator

A more realistic physical model is the damped oscillator. In this case frictional forces reduce the amplitude of oscillation. For a movement the following terms adds in the equation of motion

$$\vec{F}_r = -b\dot{x}\vec{e_x} \tag{2.11}$$

and the equation of motion is then

$$m\ddot{x} = -kx - b\dot{x} \tag{2.12}$$

With the expressions $\omega_0^2 = \frac{k}{m}$ and $2\gamma = \frac{b}{m}$ we can write the general equation of motion in the following

$$\ddot{x} + 2\gamma\dot{x} + \omega_0^2 x = 0 \tag{2.13}$$

where γ is the damping constant. Using Ansatz 2.4 leads to

$$\lambda_{1,2} = -\gamma \pm \sqrt{\gamma^2 - \omega_0^2} \tag{2.14}$$

Therefore the general solution is

$$x(t) = \exp(-\gamma t)\left[c_1 \cdot \exp\left(\left(\sqrt{\gamma^2 - \omega_0^2}\right) \cdot t\right) + c_2 \cdot \exp\left(-\left(\sqrt{\gamma^2 - \omega_0^2}\right) \cdot t\right)\right] \tag{2.15}$$

The time dependent behaviour of $x(t)$ is in particular influenced by the ratio of the

$$\frac{\text{averaged \quad restoring \quad force}}{\text{averaged \quad friction \quad force}}$$
$$= \frac{\langle|kx|\rangle}{\langle|b\dot{x}|\rangle} = \frac{m\omega_0^2\sqrt{\overline{x^2}}}{2\gamma m\sqrt{\overline{\dot{x}^2}}} = \frac{\omega_0}{2\gamma} \tag{2.16}$$

It is influenced by the relative quantities of ω_0 and γ. This can be used to determine the quality of the mechanics in subsection 2.1.4 where we will treat the three different cases separately.

In general we can observe the following system behaviours, determined by the square root in 2.14, this can be one real solution, two real solutions or two complex conjugate solutions

- For $\gamma < \omega_0$ **the under damped case** (see point 1 in subsection 2.1.4): With the following relation $\omega^2 = \omega_0^2 - \gamma^2$ we rewrite the λ parameter to
$$\lambda_{1,2} = -\gamma \pm \sqrt{-\omega^2} = -\gamma \pm i\omega \tag{2.17}$$
In that case the general solution is
$$x(t) = \exp(-\gamma t)\left[c\exp(i\omega t)\right] + c^*\exp(-i\omega t)] = A\exp(-\gamma t)\cos(\omega t + \varphi) \tag{2.18}$$
this leads to
$$A = 2|c| \tag{2.19}$$
$$\tan\varphi = \frac{-i(c - c^*)}{c + c^*} \tag{2.20}$$
Equation 2.18 describes a damped harmonic oscillation, with an amplitude A which decreases exponentially. For the boundary value $x(0) = A$ and $\dot{x}(0) = v_0$ we obtain the path-time function
$$x(t) = A\exp(-\gamma t)\cos(\omega t) \tag{2.21}$$

Together with $v_0 = -A\gamma$ we get the velocity - time function

$$v(t) = v_0 \exp(-\gamma t)\Big[\cos(\omega t) + \frac{\omega}{\gamma}\sin(\omega t)\Big] \qquad (2.22)$$

Two consecutive maxima of the damped oscillation have an amplitude ratio of

$$\frac{x(t+T)}{x(t)} = \exp\Big(-\gamma T\Big) \Longleftrightarrow \ln\left[\frac{x(t+T)}{x(t)}\right] = \gamma T = \delta \qquad (2.23)$$

where the period is $T = \frac{2\pi}{\omega}$. δ is known as the logarithmic decrement. After a time $\tau = \frac{1}{\gamma}$ the envelope

$$f(t) = A\exp(-\gamma t) \qquad (2.24)$$

of the damped oscillation is reduced to the initial value of $\frac{1}{e}$.
The angular frequency $\omega = \sqrt{\omega_0^2 \gamma^2}$ of the damped oscillation, by employing the same restoring force, is smaller compared to the case of the undamped oscillation. The frequency shift increases with more damping.

- For $\gamma > \omega_0$ **the over damped case** (see point 3 in subsection 2.1.4): The Coefficients

$$\lambda_{1,2} = -\gamma \pm \sqrt{\gamma^2 - \omega_0^2} = -\gamma \pm \alpha \qquad (2.25)$$

are real. The general solution is

$$x(t) = \exp(-\gamma t)\Big[c_1\exp(\alpha t) + c_2\exp(\alpha)\Big] \qquad (2.26)$$

With the initial condition $x(0) = 0$, $\dot{x} = v_0$ we get

$$c_1 + c_2 = 0$$

and

$$c_1 - c_2 = \frac{v_0}{\alpha}$$

This leads to the particular solution

$$x(t) = \frac{v_0}{2\alpha}\exp(-\gamma t)\Big[\exp(\alpha t) - \exp(-\alpha t)\Big] \qquad (2.27)$$

Using hyperbolic sine functions $\sinh(\alpha t) = \frac{1}{2}(\exp(\alpha t) + \exp(\alpha t))$ equation 2.23 is

$$x(t) = \frac{v_0}{\alpha}\exp(-\gamma t)\sinh(\alpha t) \qquad (2.28)$$

The oscillation consists out of only one deflection, which approaches zero for $t \longrightarrow \infty$. This case is well known as the "over damped" one

because the amplitude reaches slowly its maximum and decreases to zero. For $x(0) = A$, $\dot{x}(0) = 0$ we get

$$c_1 = \frac{\alpha + \gamma}{2\alpha} \cdot A$$

$$c_2 = \frac{\alpha - \gamma}{2\alpha} \cdot A$$

which results in

$$x(t) = \frac{A}{\alpha} \exp(-\gamma t) \Big[\alpha \cosh(\gamma t) + \gamma \sinh(\alpha t) \Big] \qquad (2.29)$$

- $\gamma = \omega_0$ ... **critically damped** (analogue to case 2 in subsection 2.1.4): In this case the parameters of our solutions are degenerate so we have

$$\lambda_1 = \lambda_2 = \lambda = -\gamma$$

We make the following Ansatz

$$x(t) = C(t) \exp(\lambda t) \qquad (2.30)$$

because equation 2.12 must have two integration - constants where $C(t)$ is a time - dependent factor, which modifies the equation of motion

$$\ddot{C} + (2\lambda + 2\gamma)\dot{C} + (\lambda^2 + 2\lambda\gamma + \omega_0^2)C = 0 \qquad (2.31)$$

For $\lambda = -\gamma = -\omega_0$ the expressions before C and $\dot{C}$ become zero, thus leading to

$$\ddot{C} = 0$$

and we get

$$C = c_1 + c_2$$

So the general solution can be written as

$$x(t) = (c_1 t + c_2) \exp(-\gamma t) \qquad (2.32)$$

2.1.3   Forced Oscillation

In this case consider the end of the spring is not free to move but it is be pushed by a periodic force. This can be written as

$$F_{drive} = F_0 \cos(\omega_{drive} t) \qquad (2.33)$$

additional forces are acting on the mass. For this setting the equation of motion is

$$m\ddot{x} = -kx - b\dot{x} + F_0 \cos(\omega t) \qquad (2.34)$$
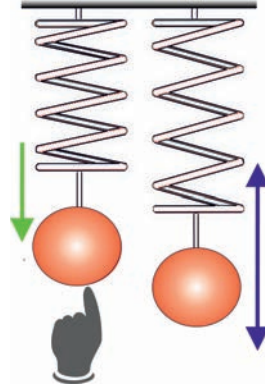
Figure 2.1: Suppose you have a mass m attached on a spring, which is periodically driven by a force $F_{drive} = F_0 \cos(\omega t)$, in the ideal case as we will see in the following chapters the force is equal to the Radiation Pressure force. The arrow on the right side points the damping due to air or any other force which is damping the system.

By inserting the following relations for the frequency

$$\omega_0^2 = \frac{k}{m} \tag{2.35}$$

damping

$$\gamma = \frac{b}{2m} \tag{2.36}$$

and external driving force in 2.34

$$F_{drive} = \frac{F_0}{m} \tag{2.37}$$

the inhomogeneous differential equation changes to

$$\ddot{x} + 2\gamma\dot{x} + \omega_0^2 x = F_{drive} \cos(\omega t) \tag{2.38}$$

 So far we allowed any periodic force for the driving force, but should underline that here we deal, in the ideal case, with the radiation pressure force. This is, see subsection 2.3.1, proportional to the optical power and to the reflection coefficient of the studied system. Actually we can rewrite equation 2.34 in the following way

$$m\ddot{x} = -kx - b\dot{x} + F_{RadiationPressure} \tag{2.39}$$

and 2.37 as

$$F_{drive} = \frac{2P(t)R(\lambda)}{c} = F_{RadiationPressure} \tag{2.40}$$

Equation 2.38 is, except for the position-independed external driving force, analogue to the equation of motion of a harmonic oscillator. The general solution of a inhomogeneous, linear differential equation is a linear combination of the general solution of the homogeneous differential equation plus a particular solution of the inhomogeneous equation.

$$x(t) = A_1 \exp(-\gamma t) \cos(-\omega_1 t \varphi_1) + A_2 \cos(-\omega_{drive} t \varphi) \tag{2.41}$$

where $\omega_1 = \sqrt{\omega_0^2 - \gamma^2}$ is the frequency of the over - damped oscillator.
For $t >> \frac{1}{\gamma}$ the first term $A_1 \exp(-\gamma t)$ is so small that it is neglectable. The second term depends on the drive frequency ω_{drive} of the driving force and determines it as the oscillation frequency. So the second term is defining the steady state. For $t \leq \frac{1}{\gamma}$ the second term describes the transient effect.

1. **steady - state**:
   Consider the steady-state of the forced oscillation where the damped transient of the system has already decayed.
   Ansatz:

   $$x(t) = A_2 \cos(\omega t + \varphi) \tag{2.42}$$

   which includes the two free parameter, the amplitude A_2 and the phase φ of the forced oscillation. If we use the Ansatz from above in the equation of motion 2.42 for solving the forced oscillations is (after using the addition theorem for trigonometric functions and sorting)

   $$\begin{aligned} &\left[\left(\omega_0^2 - \omega^2 \right) A_2 \cos \varphi - 2\gamma A_2 \omega \sin \varphi - F_{drive} \right] \cos(\omega t) \\ &- \left[\left(\omega_0^2 - \omega^2 \right) A_2 \sin \varphi + 2\gamma A_2 \omega \cos \varphi \right] \sin(\omega t) = 0 \end{aligned} \tag{2.43}$$

   This equation is valid $\forall t$, in this case we have to set the time-independent pre-factors in the squared bracket identically zero. Then 2.43 reduces to the following equations

   $$\left(\omega_0^2 - \omega^2 \right) \sin(\varphi) + 2\gamma \omega \cos \varphi = 0 \tag{2.44}$$

   $$A_2 \left(\omega_0^2 - \omega^2 \right) \cos(\varphi) - 2A_2 \gamma \omega \cos(\varphi) - F_{drive} = 0 \tag{2.45}$$

   This leads to

   $$\tan(\varphi) = \frac{-2\gamma \omega}{(\omega_0^2 - \omega^2)} \tag{2.46}$$

   For $\omega \leq \omega_0$ and $\gamma > 0$ the phase $\varphi(\omega)$ increases from 0 to $-\frac{\pi}{2}$ and for $\omega \geq \omega_0$ the phase $\varphi(\omega)$ is increasing from $-\frac{\pi}{2}$ to $-\pi$.

   In the third case when $\omega = 0$ then we know that $\varphi = 0$. In the last scenario when $\omega = \omega_0$ the phase is equal to $\varphi = -\frac{\pi}{2}$ and the maximal

value for the phase $\varphi = -\pi$ is reachable when $\omega \longrightarrow \infty$. Solving 2.34 after $A_2 \sin \varphi$ according to $A_2 \cos \varphi$ and using 2.35 leads to

$$A_2 \sin \varphi = \frac{-2\gamma\omega F_{drive}}{\left(\omega_0^2 - \omega^2\right)^2 + (2\gamma\omega)^2} \tag{2.47}$$

and

$$A_2 \cos \varphi = \frac{(\omega_0^2 - \omega^2)^2 F_{drive}}{\left(\omega_0^2 - \omega^2\right)^2 + (2\gamma\omega)^2} \tag{2.48}$$

Squaring and adding both solutions with $F_{drive} = F_0/m$ we get

$$A_2(\omega) = \frac{\frac{F_0}{m}}{\sqrt{\left(\omega_0^2 - \omega^2\right)^2 + (2\gamma\omega)^2}} \tag{2.49}$$

The amplitude of the forced oscillation depends on $F_{drive} = \frac{F_0}{m}$ the external, driving force γ the damping, ω the frequency of the driving frequency and ω_0 the resonance frequency of the driven system. In our case the cantilever´s static deflection is equal to

$$A_2(0) = \frac{\frac{F_0}{m}}{\sqrt{\omega_0^4}} = \frac{F_0}{k} \tag{2.50}$$

Here the force is turned on, which results to a bending of the cantilever. The result is again Hooke´s Law 2.1. The expression for the driven deflection at the resonance frequency ω_0 is the following one

$$A_2(\omega_0) = \frac{\frac{F_0}{m}}{2\gamma\omega_0} = A_2(0) \cdot Q \tag{2.51}$$

Differentiating the radical in the equation 2.47 after ω and setting it equal to zero gives the minimum value of the denominator. Consequently the maximum amplitude A_2 for $\omega_R = \sqrt{\omega_0^2 - 2\gamma^2}$ drifts in case of the damped oscillator, for $\gamma << \omega_0$ away.
The amplitude $A(\omega)$ in 2.47 becomes maximal for the resonance frequency ω_R when

$$\omega_R = \sqrt{\omega_0^2 - 2\gamma^2} \tag{2.52}$$

and the denominator has the value

$$2\gamma(\omega_R^2 + \gamma^2)^{\frac{1}{2}} \tag{2.53}$$

This means the amplitude at the frequencies above $\omega_{1,2}$ increases to $\frac{A_R}{2}$ with the radical in equation 2.47 the following value

$$\left(\omega_0^2 - \omega_{1,2}^2\right)^2 + \left(2\gamma\omega_{1,2}\right)^2 = 16\gamma^2\left(\omega_R^2 + \gamma^2\right)$$

this leads to

$$\omega_{1,2}^2 = \omega_R^2 \pm \sqrt{3\omega_R^2 + 3\gamma^2} \qquad (2.54)$$

The FWHM is $\Delta\omega = \omega_1 - \omega_2$

$$\Delta\omega = \left[\omega_R^2 + 2\gamma\sqrt{3\omega_R^2 + 3\gamma^2}\right]^{\frac{1}{2}}$$
$$\qquad\qquad - \left[\omega_R^2 - 2\gamma\sqrt{3\omega_R^2 + 3\gamma^2}\right]^{\frac{1}{2}} \qquad (2.55)$$

When $\gamma << \omega_R$ than

$$\Delta\omega = \frac{2\gamma}{\omega_R}\sqrt{3\omega_R^2 + 3\gamma^2} \approx 2\gamma\sqrt{3} \qquad (2.56)$$

because $\omega_{1,2}^2 - \omega_R^2 = (\omega_{1,2} + \omega_R)(\omega_{1,2} - \omega_R) \approx 2\omega_R\frac{1}{2}\delta\omega$.

The damping is limiting the amplitude A_2 to a value, where the friction energy per time unit compensates the output power, which is fed by the external driving force.

2. **transient effect**
   The system oscillates with the excitation frequency ω. The difference between ω and the eigenfrequency $\omega_1 = \sqrt{\omega_0^2 - \gamma^2}$ is determined with 2.49.

2.1.4   The Quality Factor

The quality factor describes how underdamped a resonator is. By evaluating the number of oscillations of it before the amplitude/energy drops down to $1/e$ (37 percent) of its initial value you can filter the Q - factor, which is defined for $\omega >> \gamma$

$$Q = \frac{\omega}{\Delta\omega} = \frac{\omega}{2\gamma} \qquad (2.57)$$

where ω is the resonance frequency, $\Delta\omega$ denotes the linewidth of the system and γ is the damping here. The higher the Q value is, the narrower is the resonance curve and the smaller is the damping. The following definition is equivalent to

$$Q = \pi \cdot \frac{1}{\tau} \cdot \nu \qquad (2.58)$$

where τ is the time constant of the exponential decay and ν the stored energy. The quality factor determines the behavior of the damped harmonic oscillator and the three different alternatives are (from [45]):

1. $Q > \frac{1}{2}$: The underdamped oscillator is a system that oscillates at a slightly different frequency than the free harmonic oscillator and gradually decays to zero.

2. $Q = \frac{1}{2}$:The critically damped oscillator attempts to return to its equilibrium position as quickly as possible and does this without oscillating at all.

3. $Q < \frac{1}{2}$: The overdamped oscillator also returns to its equilibrium position without oscillations but takes longer than in the critically damped case, where the Q becomes smaller, the longer it takes.

2.2   Optics

The following sections are partially taken from [38]. In many approaches laser light has to be focused or shaped with optical elements. Understanding the basics is important for the selection of the right optics. In our experiment we need to be precise with the spot size of the laser beam and shrink down the laser beam to a value smaller than $\approx 50\mu m$ in order to concentrate most of the power on the cantilever head to measure the deflection.
For this we need to understand the Gaussian beam, optics and focusing of a Gaussian beam very well.

2.2.1   ABCD Matrix and the Focusing Gaussian Beam

Matrix optics provides a modular transformation describing the effect of an optical system as a cascaded operation. For every single optical system one matrix representation exists. The description is possible within the paraxial approach. The light is explainable as ray trajectories that are described at a given meridional plane, by its height and its angle with respect to the optical axis of the system. A column comprises both parameters. The simplest mathematical object relating two vectors is a matrix. In general it is a 2x2 matrix that is usually called the ABCD matrix, because its elements are labelled as A, B, C and D.

$$\begin{pmatrix} x_2 \\ y_2 \end{pmatrix} = \begin{bmatrix} A & B \\ C & D \end{bmatrix} \begin{pmatrix} x_1 \\ y_1 \end{pmatrix} \tag{2.59}$$

where the first vector with the index 1 stands for the input ray and the index 2 for the output ray. In the following we will compute the propagation of a Gaussian beam through a lens with a focal length f in the ABCD where the lens focuses into a second Gaussian Beam locates the second waist at any point. The transformation matrix describes the ingoing and outgoing beam

$$\begin{bmatrix} A & B \\ C & D \end{bmatrix} = \begin{bmatrix} 1 & d \\ 0 & 1 \end{bmatrix} \begin{bmatrix} 1 & 0 \\ \frac{-1}{f} & 1 \end{bmatrix} = \begin{bmatrix} 1 - \frac{d}{f} & \frac{-1}{f} \\ d & 1 \end{bmatrix} \tag{2.60}$$

where $\begin{bmatrix} 1 & d \\ 0 & 1 \end{bmatrix}$ is the ABCD - matrix for free space and $\begin{bmatrix} 1 & 0 \\ \frac{-1}{f} & 1 \end{bmatrix}$ is the ABCD matrix for a thin lens.

For z we know that it is equal to a certain distance d ($<< f$) $z_1 - z_2 = d$, $z_1 = 0$ and with $z_2 = d$ the ingoing Gaussian beam at z_1 has the following waist:

$$W_1 = \frac{w_{01}^2 \pi n}{\lambda_0} \qquad (2.61)$$

For the focused waist of a Gaussian beam at z_2 we can write

$$W_2 = \frac{w_{02} \pi n}{\lambda} \qquad (2.62)$$

For the spot size we get

$$\frac{1}{W_2} = \frac{1}{W_1} \frac{\left(DA - BC\right)}{\left(A + \frac{B}{R_1}\right)^2 + \left(\frac{B}{W_1}\right)^2} = \frac{1}{W_1} \frac{1}{\left(1 - \frac{d}{f}\right)^2 + \left(\frac{d}{W_1^2}\right)^2} \qquad (2.63)$$

If $d \approx f$ we can approximate

$$W_2 \approx \frac{f^2}{W_1} \qquad (2.64)$$

By using expression (2.89) and (2.90) this leads to

$$w_{02} = \frac{f \lambda_0}{w_{01} \pi n} \qquad (2.65)$$

To focus to a small spot size you need a small λ_0, a small f but a large w_{01}. Note that $w_{02} \approx \frac{D}{2}$ is limited to the diameter of the lens diameter, the formula changes to

$$w_{02} \approx \frac{f}{\frac{D}{2}} \frac{\lambda_0}{\pi n} \qquad (2.66)$$

2.2.2 Gaussian Beams and the Knife Edge Method

The beam width can be measured using the Knife Edge method [43] recording the power. A knife edge in the beam is translated through the beam using a calibrated translation stage. The Powermeter positioned at the back of the knife records the integral of the Gaussian beam between $-\infty$ and Y the position of the knife. For the analysis we look at the propagating beam in z-direction with a Gaussian intensity profile:

$$I(x.y) = I_0 \exp\left(\frac{-2x^2}{w_x^2}\right) \exp\left(\frac{-2y^2}{w_y^2}\right) \qquad (2.67)$$

where $w_x, w_y = \frac{1}{e^2}$ are the radii of the beam in x-, y- direction and I_0 is peak intensity. The total power in the beam is given as

$$P_{FULL} = I_0 \int_{-\infty}^{\infty} \exp\left(\frac{-2x^2}{w_x^2}\right) dx \int_{-\infty}^{\infty} \exp\left(\frac{-2y^2}{w_y^2}\right) dy = \frac{\pi}{2} I_0 w_x w_y \quad (2.68)$$

The transmitted power is given as

$$P(x) = P_{FULL} - I_0 \int_{-\infty}^{X} \exp\left[\frac{-2x^2}{w_x^2}\right] dx \int_{-\infty}^{\infty} \exp\left[\frac{-2y^2}{w_x^2}\right] \tag{2.69}$$

where P_{FULL} is a known solution so it will be subtracted from the partially from the knife covered part.

$$P_{FULL} - P_{Powermeter} = P_{reflected} \tag{2.70}$$

P_{FULL} is the solution of the integral plus the known solution, $P_{Powermeter}$ that is the integrated part, and $P_{reflected}$ this is the missing part.

$$P(x) = P_{FULL} - I_0 \int_{-\infty}^{x} \exp\left[\frac{-2w^2}{w_x^2}\right]$$
$$= P_{FULL} - I_0 w_y \sqrt{\frac{\pi}{2}} \frac{\sqrt{\frac{\pi}{2}}\left(1 + Erf\left[\sqrt{2}p\sqrt{\frac{1}{w_x^2}}\right]\right)}{2\sqrt{\frac{1}{w_x^2}}} \tag{2.71}$$

This leads to the final solution

$$P(x) = \frac{P_{FULL}}{2}\left[1 - erf\left(\frac{\sqrt{2}p}{w_x}\right)\right] \tag{2.72}$$

The function can be written as

$$P_{measured} = \frac{Pow}{2}\left(1 \pm erf\left(\frac{\sqrt{2}X - Pos}{R}\right)\right) \tag{2.73}$$

where Pow is the optical power, R radius of the Gaussian beam $(+/-)$ when the knife is translated in the negative / positive direction and Pos position.

2.3   Quantum Physics

Light has interesting properties. One is that light consist of particles and that light behaves like a wave. In fact experiments and the theory showed that this conclusion was right. Photons can be seen mathematically in both pictures at the same time. In the following we restrict ourselves to the particle picture.

2.3.1   Radiation Pressure Force

The radiation pressure force results ([39]) from the photon momentum upon a reflective surface $2\hbar|\vec{k}|$, where $\hbar$ is the Plank Constant. The force is

$$F_{RadiationPressure}(t) = \frac{2P_{optical}(t)R(\lambda)}{c} \tag{2.74}$$

with the $P_{optical}(t)$ is the optical power of the laser, which is time - depended, $R(\lambda)$ (see the following chapter 3) the wavelength depended reflectance coefficient of the mirror over the speed of light c. Let´s assume that the surface is a high reflective one so $R(\lambda) = 1$ and neglect it for the sake of simplicity. Before we start with the short deviation remember those definitions :

$$\lambda = c\nu \tag{2.75}$$

for the wavelength and the following equation for the energy of photon is defined as

$$E_{Photon} = \hbar\omega = h\nu \tag{2.76}$$

According to Newton's second law and by using the formulas 2.75 and 2.76 from above we get

$$|\vec{F}| = \dot{p} = \frac{\Delta p}{\Delta t} = \frac{2\hbar|\vec{k}|N}{\Delta t} = \frac{2NE_{photon}}{\Delta t} = \frac{2P_{optical}}{c} \tag{2.77}$$

where N denotes the number of photons.

Chapter 3

Micro Mirror Design

This chapter will focus on the properties of the micro mirrors and explain the meaning of DBRs as well as the mechanical design goals. This part of the thesis gives an introduction to the interesting features of distributed Bragg reflectors and justifies why these are interesting candidates for the demonstration of the radiation pressure force.

3.1 Requirements for the micro mirrors

At this point we will give a brief review of the requirements for mechanical and optical interaction of the tested cantilevers.

A low spring constant is advantageous for the radiation pressure test, this can be reduced by reducing the mass. The shape and geometry of the cantilevers can be modeled such that this requirement is fulfilled. Profitable here are cantilevers with long beams of approximately few milimeters. See also section 3.4.

Due to the experimental setup, (see 4) the cantilever needs to be accessible from the front and rear side. For this we had to expose the micro mirrors with the combination of etching techniques 3.4.3, without reducing the reflectivity level of 99.99% on both sides.

Challenging in this radiation pressure experiment is the demonstration of this effect without the need of sophisticated and indirect measurements.

So in our case, it would be beneficial to reduce the absorption rate significantly. We have succeeded in this by growing the whole structure on a *GaAs* substrate.Section 3.4 contains more detailed description of the system under study.

3.2 Distributed Bragg Reflectors (DBR)

Distributed Bragg reflectors (DBR) or Bragg mirrors are dielectric mirror structures based on Bragg reflection. DBRs consist of alternating layers of

two different optical materials. The refractive indices alternate periodically between two fixed values: n_{Low} and n_{High}. Each optical layer corresponds to one quarter of the wavelength for which the mirrors are designed. These specifications are effective only for normal incidence.

The reflectance of a DBR can be determined by the following expression [44]:

$$R = \frac{1 - \left(\frac{n_{High}}{n_{Low}}\right)^{2N} \cdot \frac{n_{High}^2}{n_a n_b}}{1 + \left(\frac{n_{High}}{n_{Low}}\right)^{2N} \cdot \frac{n_{High}^2}{n_a n_b}} \tag{3.1}$$

where n_a corresponds to the input medium, which is in most cases air and therefore is $n_a = 1$, and n_b is the output medium. The reflection bandwidth is determined mainly by the index contrast. Figure 3.1 shows the reflection curve of our cantilevers with respect to the wavelength. This can be generated by using the transmission matrix approach. We used the VERTICAL software package, which was originally made for the design and simulation of Vertical-Cavity Surface-Emitting Lasers (VCSEL) (see also [41]). In [40], the authors analyse DBRs and give exact expressions for some of their properties.

Each layer, between the micro-mirror front and rear, contributes to a Fresnel reflection. The reflected light from every layer interferes constructively and results in a strong reflection.

These quarter-wave structures are also very basic building blocks of more complicated dielectric mirror structures (see [44]).

3.3   Types of Bragg Reflectors

DBR´s can be fabricated with different technologies [42]:

1. Dielectric mirrors based on thin-film coating evaporative technology, ion beam sputtering or epitaxial growth are used as laser mirrors in solid state bulk lasers. The mirror structure then consists of amorphous or crystalline materials. Mostly these are used for vertical illumination. In our radiation pressure demonstration, we use cantilevers from this category.

2. Fiber Bragg gratings, including long-period fiber gratings, are often used in fiber lasers and other fiber devices. They can be fabricated by irradiating a fiber with spatially patterned ultraviolet light. Similarly, volume Bragg gratings can be made in photosensitive bulk glass.

3. There are various types of Bragg reflectors used in other wave guides, based on, for example, corrugated waveguide structures which can be
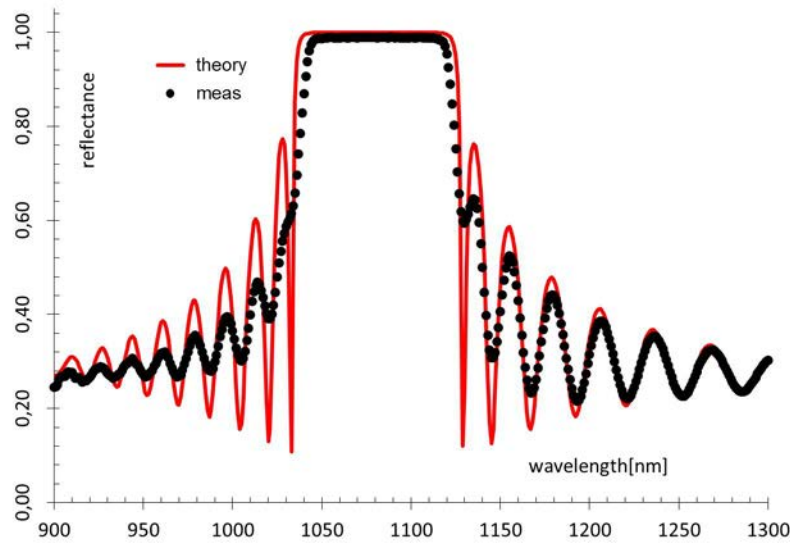
Figure 3.1: The red solid line is the reflectance curve modelled with VER-TICAL. The black dots are measured with the spectrophotometer. The dips do not go to zero due to the limited resolution of the system. Thanks to Garrett D. Cole for giving the measurement results.

fabricated via lithography. Such gratings are used in distributed Bragg reflectors or distributed feedback laser diodes. Additionally, these are used for horizontal (or in-plane) illumination. Such realizations are called "on chip" designs.

3.4 Microoptomechanical Systems (MOMS)

3.4.1 Design Description

The cantilevers are etched on a $7mm$ wide and $7mm$ long square chip, which is a layered stack material of $Al_{0.12}Ga_{0.88}As$ layer with a high refractive index layer ($79.4nm$) and $Al_{0.92}Ga_{0.087}As$ ($90.4nm$) with low refractive index, followed by a $271nm$ thick $Al_{0.92}Ga_{0.087}As$ etch protection layer. The layered stack material is grown on a $GaAs$ (100) substrate.

The micro machined structures are good for our purpose because they have low absorption, averaging between 50 to 70ppm over the wavelength range $900nm - 1300nm$, and this minimizes radiometric or photothermal (bolometric) forces. This was tested from SPTS[1] with a spectrophotometer.

The reflectivity of these structures is, on both sides, $> 99,99\%$. In 3.1 you

---

[1] Measured by Alexei Alexandrowski, Stanford Photothermal Solutions, Hawaii, USA
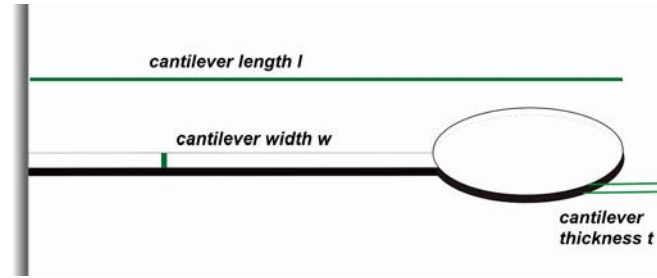
Figure 3.2: This is a schematic side-view of a cantilever freely moving in air. The cantilever is created the way a diving-board is anchored over the edge of a swimming pool. The relevant quantities for formula 3.2 are marked in blue.

can see how the reflectance curve is modeled on the computer at different wavelengths; for our measurements the relevant range is between 900 nm and 1300 nm.

These low-stress epitaxial materials enable the construction of very high aspect ratio devices with negligible strain-induced deflections.

The low-mass and low-stiffness cantilevers are presented in 3.3. The stiffness of a resonator can be reduced maximally when the cantilever is fixed only on one side as we do here. Fixing both sides makes it less likely for the photons to excite the micron beam around micrometers, these would have a smaller displacement which would be harder to detect. Additionally the structure itself is stiffer, this results in higher spring constants.

We can calculate the spring constant from the geometric values and material properties. This formula depends on the geometry of the cantilever beam, in this case for a rectangular beam (see [46])

$$k_{Calc} = \frac{E \cdot w \cdot t^3}{4 \cdot l^3} \tag{3.2}$$

where E is the Youngs modulus, w is the width of the cantilever, t is the thickness of the cantilever, l is the length of the cantilever. See 3.2.

The cantilever has a round head in order to maximize the interaction region with the laser spot. We know already from the Gaussian Beam chapter that almost 86% of the beam intensity of a Gaussian beam (see 2.2) will be incident on the cantilever, when the radius of the beam is equal to the diameter of the cantilever head. The beam size is limited mostly by the lens construction. We use to focus the beam waist to $\approx 20\mu m$ depending on the wavelength.

Secondly a round head allows us to lower the cantilever´s mass. It is not necessary to use a square cantilever head, the round design allows proper beam focusing and reduced mass compared to a cantilever which has a square

A-cantis, 3 mm long, left to right
1) width: 5 um, pad diam: 50 um
2) width: 10 um, pad diam: 50 um
3) width: 20 um, pad diam: 50 um
4) width: 5 um, pad diam: 100 um
5) width: 10 um, pad diam: 100 um
6) width: 20 um, pad diam: 100 um

B-cantis, 1.5 mm long, left to right
1) width: 5 um, pad diam: 50 um
2) width: 10 um, pad diam: 50 um
3) width: 20 um, pad diam: 50 um
4) width: 5 um, pad diam: 100 um
5) width: 10 um, pad diam: 100 um
6) width: 20 um, pad diam: 100 um

C-cantis, 2 mm long, left to right
1) width: 5 um, pad diam: 50 um
2) width: 10 um, pad diam: 50 um
3) width: 20 um, pad diam: 50 um
4) width: 5 um, pad diam: 100 um
5) width: 10 um, pad diam: 100 um
6) width: 20 um, pad diam: 100 um

D-cantis, 1 mm long, left to right
1) width: 5 um, pad diam: 50 um
2) width: 10 um, pad diam: 50 um
3) width: 20 um, pad diam: 50 um
4) width: 5 um, pad diam: 100 um
5) width: 10 um, pad diam: 100 um
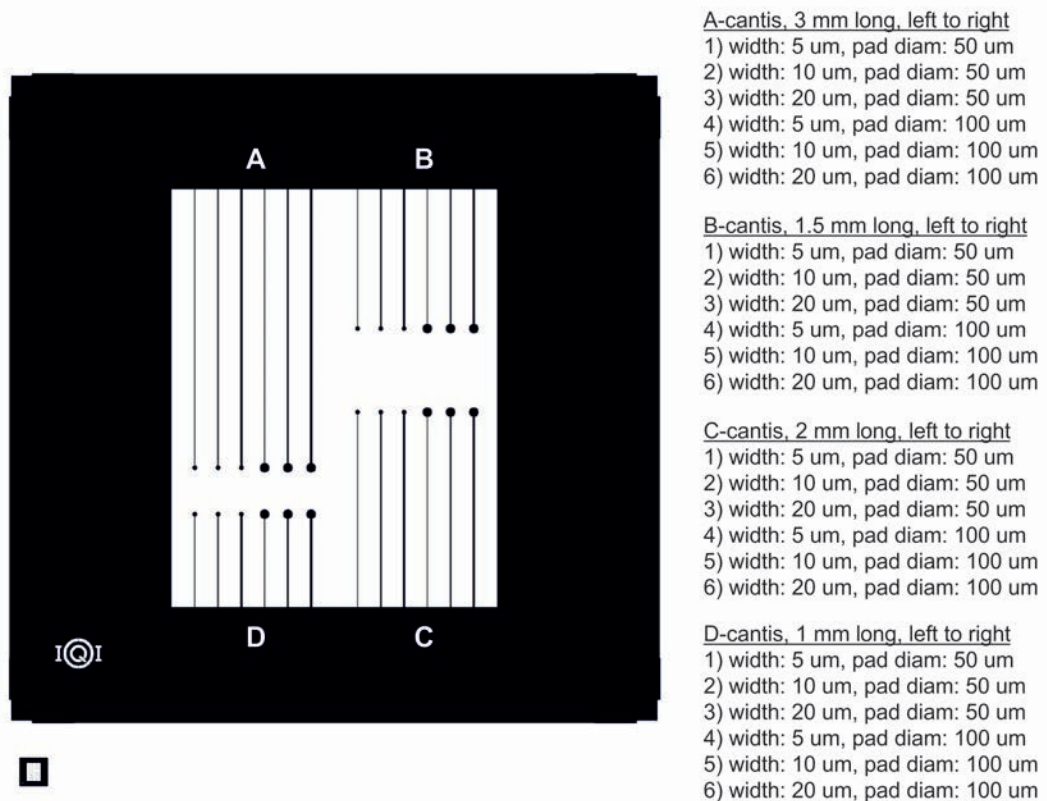6) width: 20 um, pad diam: 100 um

Figure 3.3: This picture shows the whole chip with its single cantilevers. This is originally made for the etching mask which will be overlay during the fabrication process to etch the cantilevers an the high quality stacked thin film layers. This is done by Garrett D. Cole
The small black square shows the chip with the cantilevers in the original dimension (7x7 mm).

head[2]

3.4.2   Mechanical Design

24 cantilevers are on the chip, as shown in figure 3.3. These are divided into four different blocks, each with a different arm length: $1mm$, $1.5mm$, $2mm$ and $3mm$ for blocks A, B, C, and D respectively.
For each arm length cantilevers are produced with arm thickness of $5\mu m$, $10\mu m$ and $20\mu m$ The cantilever heads are $100\mu m$ and $50\mu m$ in diameter. These cantilevers have low resonance frequencies, which depend on the geometry. Those with the shortest arm ($1mm$) are the stiffest with resonant

---
[2]Design was made by Garrett Cole in collaboration with Thomas Corbitt from MIT.
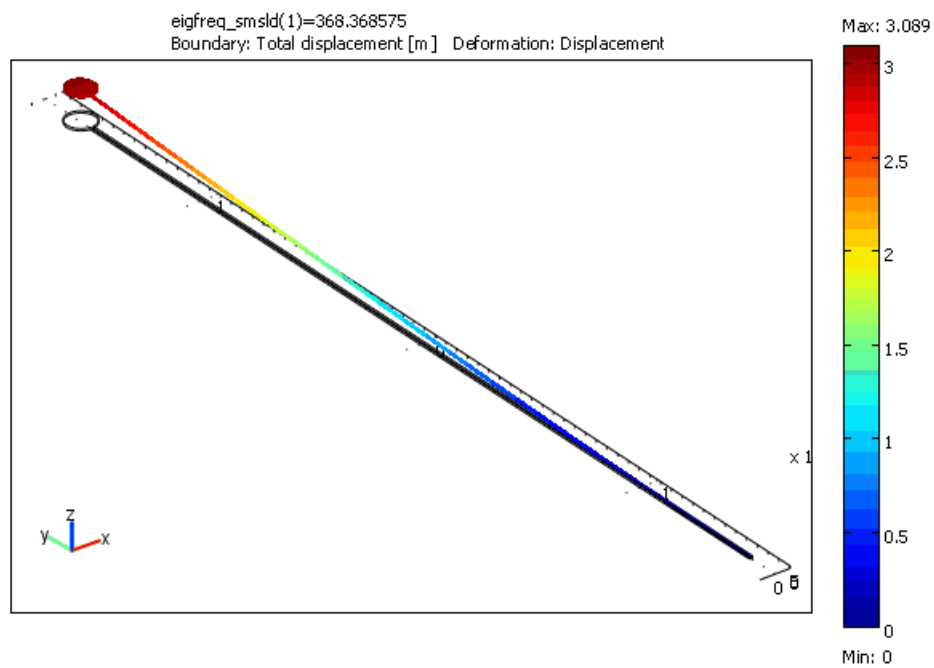
Figure 3.4: This picture shows the out-off-plane motion of a cantilever excited by a modulated periodic force. The red areas are those where the stress is high compared to the blue areas where the stress on the cantilever is lower. Compare the colour bar on the side.
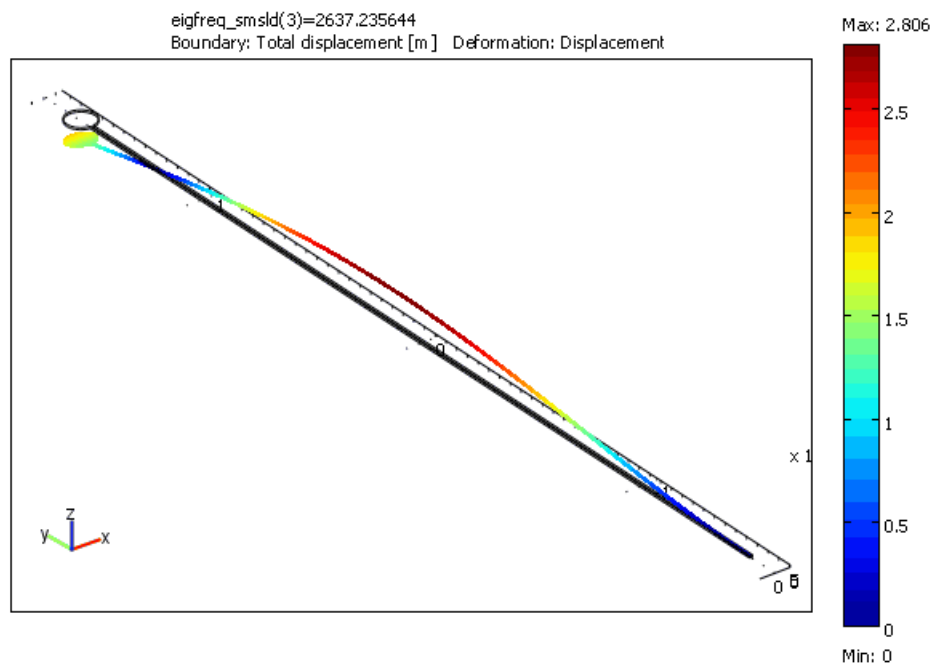
Figure 3.5: This picture shows the higher mode. This was simulated with COMSOL.

frequencies around $1kHz$. In contrast, cantilevers with an arm of $3mm$ have resonant frequencies of $\approx 300Hz$. Due to the low frequency range $300Hz - 1kHz$ our cantilevers are sensitive to acoustic noise. In subsection 4.3.8 present the results, when we drove the cantilevers acoustically.

Figure 3.4 and 3.5 show the first and second out-of-plane modes with a color bar to indicate the severity of the cantilever's bending.

For fabriaction we use a similar process to [53]; for a detailed description see 3.4.3.

3.4.3 FEM - Model

We use the finite element (FEM) simulation software (COMSOL Multi-physics) to analyse the mechanics before we fabricate them. This gives us information about the frequency and mass.

Complex systems can also be modeled to solve practical issues because analytical models are sometimes not solvable or just to complicated to solve. Then numerical simulation can be helpful to study the behaviour of the mechanical device. At the same time it is an efficient way to find the eigen-functions of resonators with complicated geometries.

We also analyse the higher order modes to find out how the cantilever behaves at different frequencies and how thermal forces can change the motion of such a cantilever.

Effectively it gives us the solution for the frequency of the device, the effective mass (mass falls into weight when the beam is moving - instead the effective mass itself is the one which gives the whole mass of the complete cantilever) and the proper spring constant values.

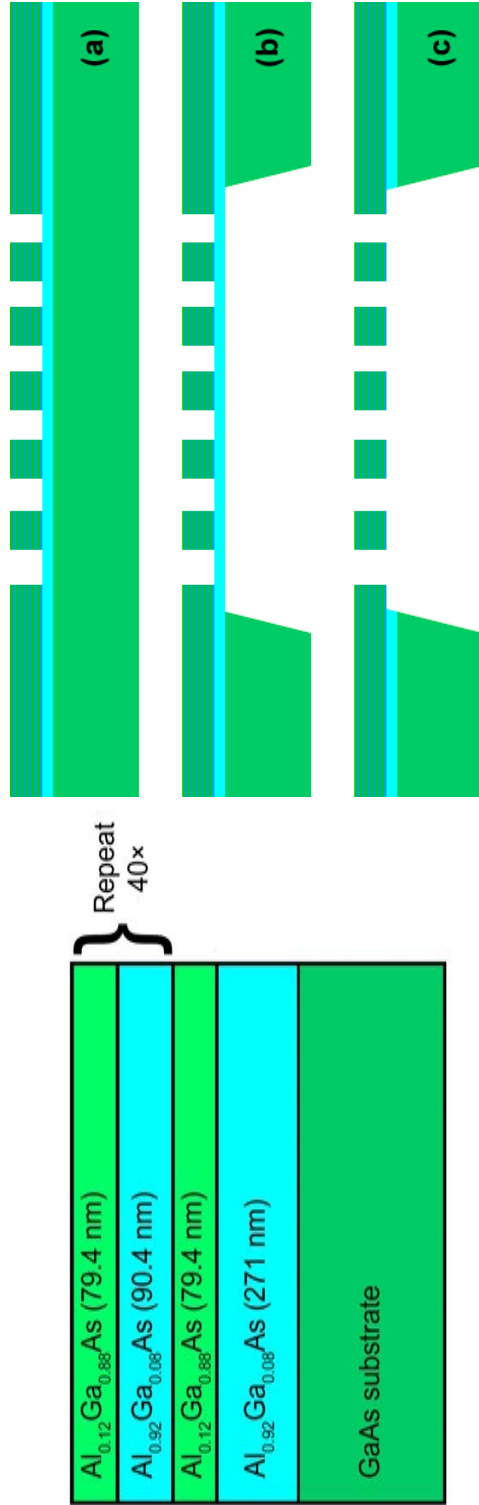The design is drawn in SolidWorks and imported into the FEM software.

Figure 3.6: From left to right: (left) Here the structure of the cantilevers is shown with the two different layers and the substrate. (right) The cantilevers consist of alternating quarter-wave $Al_{0.12}Ga_{0.88}As$ (high index) and $Al_{0.92}Ga_{0.08}As$ (low index) layers, followed by a 271nm thick $Al_{0.92}Ga_{0.08}As$ etch-protection layer, on a $GaAs$ (100) substrate. The high Al-content layer below the Bragg stack acts as an etch stop for the through-wafer etch.(right) Fabrication of the cantilevers relies on a bulk micro machining process whereby (a) the lateral dimensions are defined by lithographic patterning and plasma etching through the DBR ($\approx 7\mu m$ in depth). (b) A backside window is opened via wet-chemical etching of the GaAs substrate (thinned to $200\mu m$).(c) The cantilevers are made free-standing by the removal of the etch stop layer.

Chapter 4

Experimental Realization

In this chapter the experimental set-up (see figure 4.1 and picture 4.2) is presented and the measurements are described in detail. Besides, the results are shown in subsection 4.3

4.1 Experimental Set-up

The set-up consist of three independent arms (see figure 4.1) :

1. Readout arm (red area): Measures the displacement of the cantilever.

2. Driving arm (green area): Excites the cantilever with optical pulses.

3. Imaging arm (yellow area): Pictures the cantilevers with a CCD (Charged-Coupled Device).

Independent measurements of the different arms are possible. For example the sensitivity measurement (see for a detailed description subsection 4.1.1 and for results 4.3.3) can be measured, independently, on the Readout arm. However, the static reflection (see 4.3.5) only needs the Driving arm. The remaining measurements, such as the radiation pressure test (4.3.6), the spring constant test (see 4.3.7) and the measurements for characterizing the mechanical properties such as the ring-down measurement or the resonance curve 4.3.4 (for example Q-factor and/or frequency ν), need both arms. Results are shown in section 4.3.

4.1.1 Readout Arm

For our table-top radiation pressure demonstration, we used the optical lever method to analyse the position displacement of the driven cantilever, which is shown in figure 4.3. The beam deflection technique is commonly used in Atomic Force Microscopy (AFM) and includes a light source, focusing optics,
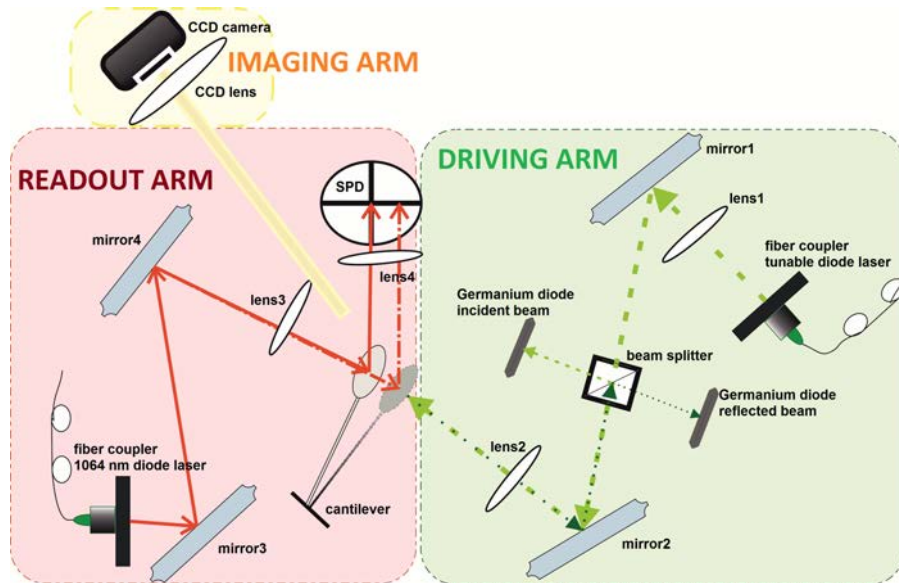
Figure 4.1: This is a sketch of the experimental set-up, without the optical Chopper in the Driving arm. The set-up is divided into three separate arms: Readout arm (red), Driving arm (green) and Imaging arm (yellow).
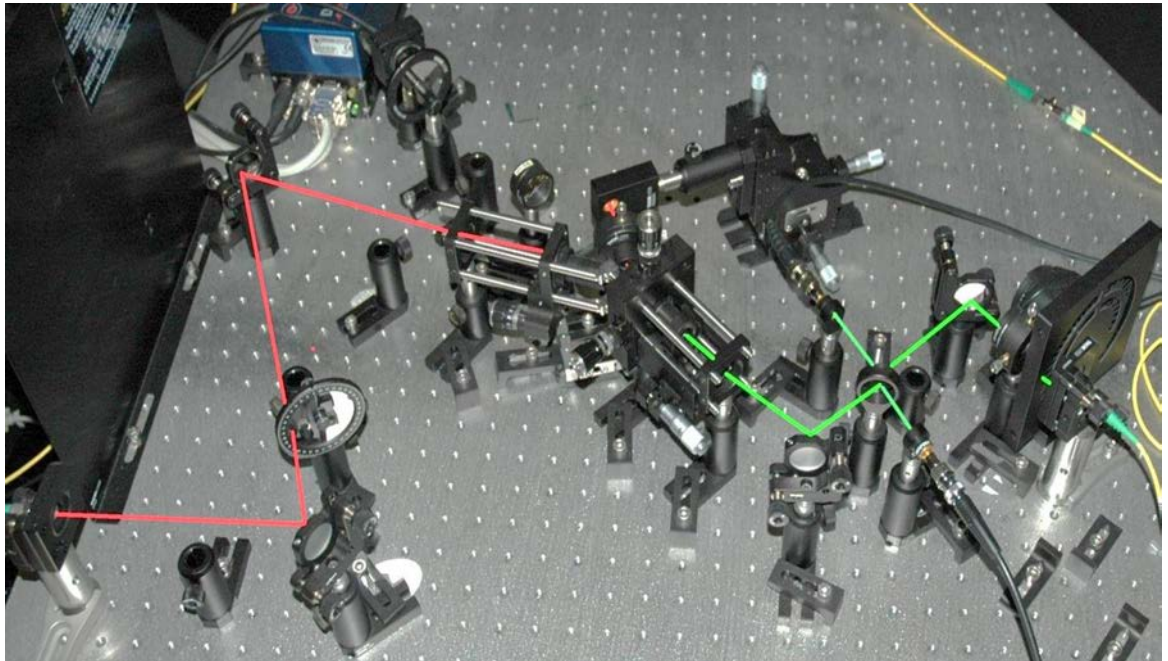

Figure 4.2: This picture shows the experiment, which was used for the measurements in air.
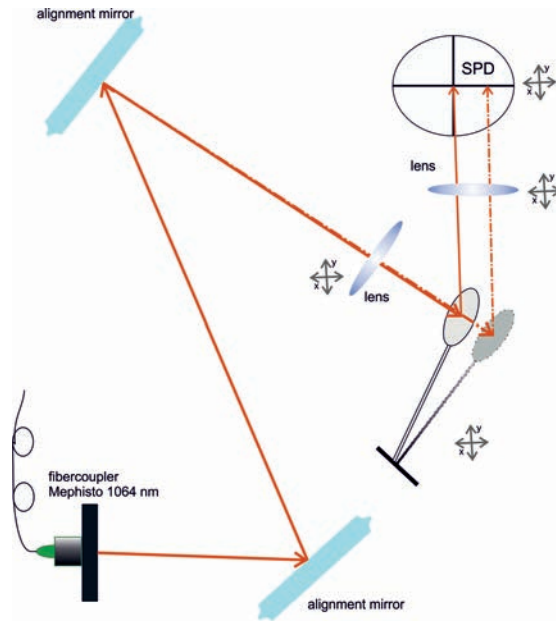
Figure 4.3: The Readout arm.

and a detecting system. The detector provides the necessary high sensitivity for the measurement of micron cantilever displacements. For detailed information see [31]. The sensitivity measurement is performed on this arm. For this measurement the linear range of the split-photo diode (SPD) determines the conversion factor of the motion of the laser spot, with respect to the position of the laser spot, at the SPD. Of the resulting linear part of the measurement, we are interested in the values of the slope. In order to catch the linear part, we kept the laser source fixed and aligned the laser spot on the cantilever. The reflected beam is directed to the SPD, which is fixed on a translation stage. The smallest increment of the micro meter screws on the stage is 10 μm. This gives us the accurate position values for the side-to-side motion of the stage. If the beam is well aligned, homogeneous and round, then we should see high values on the the (difference) DIFF-channel. This should reach a maximum point, go through zero, then reach a minimum point. For details see 4.3.3
Figure 4.4 is an example of the full-sensitivity curve. The signal crosses the zero line, reaches a maximum value, drops down to a minimum point and goes back to zero after leaving the detecting area. The pictures in the graph in 4.4 shows the laser spot position on the SPD which is divided into four segments. The arrows on the side are pointing to the measured values at the SPD. In the first picture the spot covers the left side (segments Q2 and Q3) of the SPD. The arrow above points to a measured value and than is the amplitude maximal.

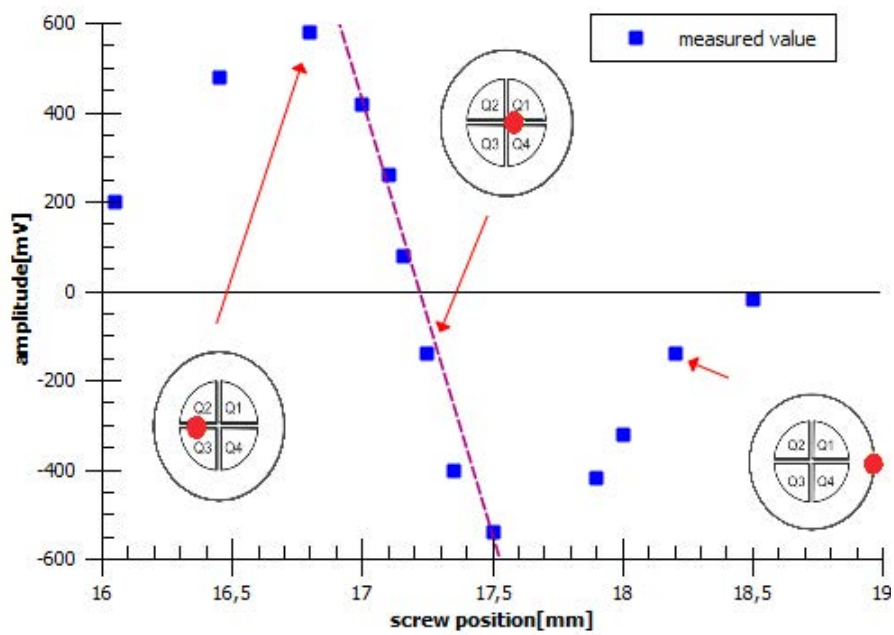Figure 4.4: This figure shows the linear and non-linear SPD response when it is translated from left to right. The linear part contains all the points along the dotted violet line. The pictures on the side corresponds to the different laser beam and SPD positions, arrows are pointing to the measured values. The left-right configuration, $[(Q_2 + Q_3) - (Q_1 + Q_4)]$, is used for the measurements.

In picture 2, the laser spot is on the left side of the SPD center and negative values are measured. The arrow points to the measured value. When the spot is leaving the detecting area, the measured voltage is already zero. This shows the third picture. The arrow points again to the measured value.

Fiber: In the whole set-up APC/FC (angled physical contact/ fibre channel) fibers, with an angle polished tip under 8° are used. This feature is advantageous, the values for back reflections are significantly reduced with high return losses greater than 60 dB.
Such back-reflections can cause instabilities on the Driving arm in the cavity of the tunable laser Toptica DL Pro, where a tuning from 990 nm to 1100 nm is necessary for the Radiation Pressure test with respect to the wavelength. This is not so critical for the Readout arm, where the wavelength is fixed, to 1064 nm the wavelength of the Mephisto laser.
Besides, all the optical elements are C-coated, broadband anti-reflective (AR) coating for the wavelength range 1050 nm - 1620 nm.

Optical Table: The optical table, where the set-up is fixed, is made by Thorlabs Company (PBI 52515 Performance Plus Breadboard). It is 1200 mm long, 900 mm wide, with a thickness of 110 mm.
The whole set-up is resting on a self-levelling frame with an active damping [47].
The used table is mounted on air springs, to prevent the coupling of ambient background vibration. Vibration isolation supports and vibration isolation frames are designed to isolate the optical table and optical breadboard, respectively, from ambient vibrations in the building, which are typically in the 4 Hz to 100 Hz range, since large frequency differences exclude energy transfer from one form into another.

Mephisto Laser: The laser diode on the Readout arm is the Mephisto laser manufactured by Innolight GmbH working at the fixed wavelength of 1064 nm. The emitted laser power is controlled with a tunable attenuator.

Fiber Coupler: The fiber couplers (F240APC-C) in the set-up are from Thorlabs Company. The collimation lens with a focal length of 8.13 mm inside the fiber coupler is used in the experiment to create collimated laser beams.

Alignment mirror 1 and 2: For precise alignment on the 100 μm - 50 μm cantilever heads, two silver coated are implemented. These alignment mirrors are 1 inch in diameter. The additional levelling screws are useful during alignment and positioning of the laser spot.

Lens and Cage System: Before the laser light hits the cantilever heads,

we inserted a lens with a focal length of 25 mm. The lens shrinks the waist of the laser beam down to $\approx 20\ \mu m$ in front of the MOMS structure (cantilever head).

Mirror and Mirrorholder (Translation Stage): In the beginning, we screwed the chip between the micro-mirrors on a low-profile compact kinematic mirror mount and a metal strip. This was not a good way to mount the micro mirror. The fragile MOMS structure alignment was crucial.

To avoid this problem, we design a custom made holder for the chip (see 4.5). The chip holder itself has a diameter of 1 inch because the holder will be fixed inside a Thorlabs translation stage (ST1XY-D).

The lens holder (see figure 4.5) was designed to connect to 30 mm cage assemblies. The holder consist of two assembly parts. The first component, made out of aluminium, has a thickness of 9 mm. This element has a recess of $\approx 7\ \mu$m, approximately the same thickness as the chip, and a round chip opening to position the chip better on the round aluminium supportive part. The upper assembly part is 1 mm thick and made out of Teflon. It has half of the diameter of the lower structural element. This part has also the round chip opening, for free access to the MOMS structures. The function of the upper assembly was to keep the chip in the middle and apply a small but enough force on it, when it is vertically clamped into the lens holder.

All the parts, including the chip, are fixed with M2 screws.

The left and the right side of the custom-made chip holder are fixed together with metal retaining rings inside the threaded translation stage (ST1XY-D, Thorlabs Company). This apparatus makes alignment more convenient. The micrometer screw makes coarse translations of 400 μm per cycle and fine translations (25 μm per cycle). With this holder precise adjustments without tilting the micro-mirrors is possible.

The laser spot of the Driving arm is fixed at a random position. For the localisation we scattered the spot. Then the laser spot of the Readout arm was moved to the same position. The cantilever head is moved with the help of the micrometer screws on the stage between both spots. The laser spot on the Readout arm is now pointing in the direction of the SPD and the laser spot of the Driving arm is reflected back through the beam splitter on the Germanium diode.

Lens: We decided to queue a second lens right after the cantilever. This one collects all the reflected light from the MOMS device and re-collimates the laser beam before it hits the split photo diode.

When the spot size is bigger than the cantilever motion, then a distinction between cantilever *zero position* (unloaded position) and cantilever *moved position* (loaded position) is not possible.

To catch the right distance from the lens it is bolted on a small translation stage with a 5 mm long translation screw. The focal length of the lens is 25
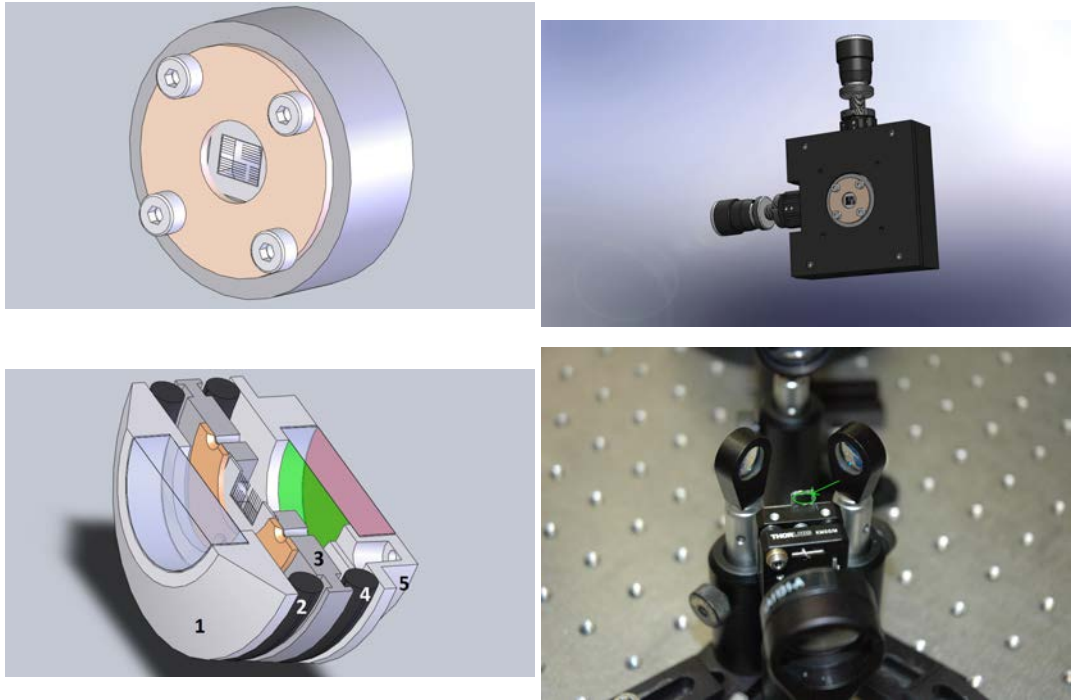
Figure 4.5: From top-left to bottom-right: (top-left)This the chip holder, designed in SolidWorks (Thanks to Garrett D.Cole who drew parts of the holder and chamber in SolidWorks) which we used for our air measurements. This holder was fixed inside the translation stage (next picture), (top- right) Again the holder with the MOMS chip inside fixed in the translation stage. (bottom-left) A lateral cut the mini-vacuum chamber, which we employed for the vacuum tests. The numbers corresponds to the description in 4.2. (bottom-right) Fixing of the cantilevers on top of the kinematic mount. This holder was the first one for the first air tests, where we clamped the chip between the holder and a metal strip.
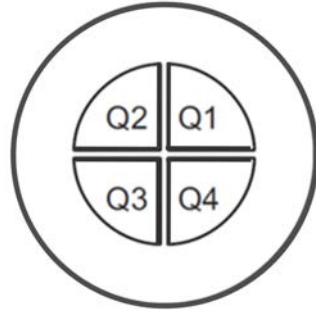
Figure 4.6: *Split photo-diode* consisting out of four independent diodes better known as quadrants. In the literature this kind of diodes have different synonyms such as *Segmented photo-diode* or *Quadrantdiode*.

mm. For Results see subsection 4.3.2.

Split Photodiode (SPD): A position - sensing detector is a photoelectric device that converts light into continuous position data. The SPD is divided into four segments or quadrants (see 4.6), where each of them is an individual photo diode. The used SPD [1] is PDQ30C from the Thorlabs company with a Indium - Gallium - Arsenide (InGaAs) photo-diode. The SPD works within the infrared range (IR) or the wavelength range between 1000 nm to 1700 nm. According to the manual, optimal is a spot size less than 0.5mm. The SPD will work with wider spot sizes but for best results the spot should be located within 80% in the center of the detector. The X-axis and Y-axis signals are proportional to the light difference sensed by the left-minus-right $(Q2 + Q3) - (Q1 + Q4)$ and top-minus-bottom $(Q1 + Q2) - (Q3 + Q4)$ pairs of photo diode elements in the detector array. The sum(SUM)-signal is proportional to the total amount of light falling on the sensor. The maximal power striking the SPD depends on the wavelength and is, according to the manual, between 1.3 mW to 1.4 mW (see 4.3.3).

4.1.2 Driving Arm

This arm excites the cantilever periodically with optical pulses. 8 % of the incident beam, from the tunable DL Pro laser, and reflected beam, from the cantilever head, splits the laser beam and is controlled with the Germanium diode. (The reflected beam corresponds to the Germanium diode on the left of the beam splitter in figure 4.7.)
For the Driving arm, an independent diode laser, tunable from 990 nm to
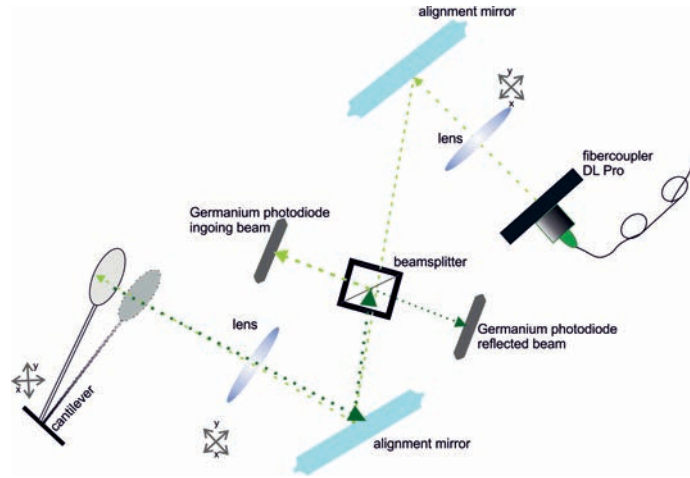
---

[1]from the Thorlabs Manual

Figure 4.7: This is the Driving arm of the experimental set-up.

1100 nm, is in use.

The tunable laser is important for the demonstration of the radiation pressure test 4.3.6.

In order to drive the cantilever properly, the laser beam has to be focused on the cantilever. The beam waist (see 4.3.2) is measured with the Knife-Edge method (see subsection 2.2.2). We checked the position and the diameter of the waist at different wavelengths, starting from 990 nm to 1100 nm in 10 nm steps.

For this, we insert a pre-focusing lens after the fibre coupler, which is positioned 41.5 mm ±0.5 mm away from the second focusing lens. The waist is measured at four different positions.

The Driving arm gives information about the material response (static measurement - see 4.3.5). This measurement extracts additional information, such as the reflectance level at different wavelengths.

DL Pro: This laser source was manufactured by TOPTICA Photonics. The tunable range starts from 990 nm to 1100 nm. The Littrow geometry (grating outside the laser cavity) in the DL Pro laser allows precise wavelength changes. The grating angle adjustment, for changing the wavelength, is operated by a stepper motor which can be controlled either manually by potentiometers on the MOT/DL pro Control Box or by computer via the supplied LabView based Control Software. The stepper motor operation ensures wavelength changes with an accuracy of typically ±0.2 nm.

The DL Pro is extremely sensitive to temperature changes and instabilities of the table. Then the power changes and realignment is necessary.

Interesting is that the DL Pro can not be calibrated constantly high at all wavelengths, which would be convenient for data analysis. Instead nor-

malization is required on the intensity of the ingoing beam of the DL Pro, measured with one of the photodiodes and the measured amplitude on the SPD.

Fiberdock: The Fiber Dock is for fiber coupling of single mode fibers which uses only APC/FC connections as a standard solution. It couples the laser beam into a single mode fiber. An internal lens is optimized for the wavelength of the DL Pro laser head. Realignment is necessary, when the fiber is removed from the Fiberdock.

Beam splitter and Germanium photo diodes: The beam splitter, a very thin glass plate, is positioned between the alignment-mirrors.
In general, glass plates are reflecting 4%, [34] this means there is always a reflection on the front and back surface of such a glass plate on both 4%. Both spots are distinguishable depending on the thickness of the plate. The glass plate, in the set-up, is so thin that the front and back reflections are overlapping and this results in the 8% (double reflection). The Germanium diodes (SM05PD6A) are high speed photodiodes. The spectral response goes from 800 nm to 1800 nm and has an active area of 3 mm.
These are helpful for controlling the power level of the ingoing laser beam and for measuring the reflected beam.

Lens and Cagesystem: The appropriate lens construction (see figure 4.1.2) generates, depending on the wavelength, laser spots between 16 μm and 20 μm in diameter. Here the laser beam is pre-focusing before the light passes through the second lens, to the MOMS structure, to reach the above mentioned values.
We integrate a cage system, consisting of four rigid steel rods, on which optical components can be mounted along the optical axis. This makes the alignment of the lenses easier.

Light Modulation: The light is shaped by the New Focus Model 3501 optical chopper. It is designed to interrupt light paths in optical experiments at frequencies from 4 Hz to 6.4 kHz.
For the intensity modulation the 60 slot chopper blade is used for the test because the frequency region of the cantilever is perfectly covered.

4.1.3   Readout and Driving Arm

This subsection gives a list of all the measurements where both arms are needed.

- The resonance curve measurement 4.14 :
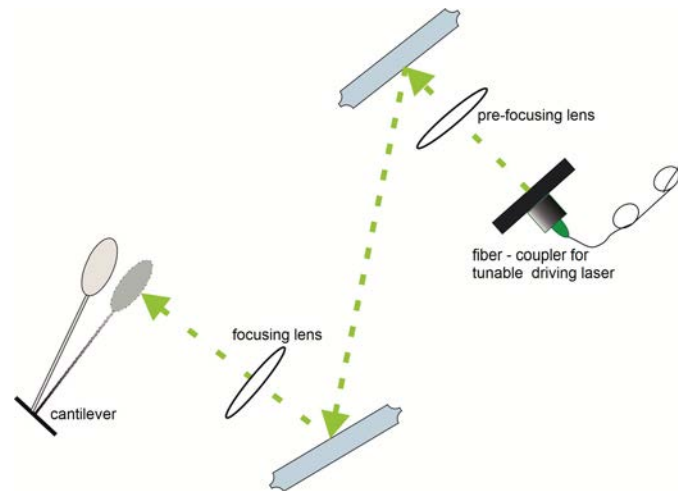 Here the chopper is turned on, during the frequency scan around the

Figure 4.8: This picture sketches the lens configuration of the Driving arm. The pre-focusing shrinks the waist diameter before the beam is directed through the focusing lens to the cantilever. Here we ignore the back-reflection from the cantilever surface, for now.

geometry-specific frequency spectrum. As a reference, for the right frequency span, we scan around the resonance frequency. The COMSOL-software simulation calculates the frequency depending on the geometry of the cantilevers 3.4.3. Any change of the amplitude is analysed at the SPD. Expected is a high peak at the resonance frequency. In air the cantilevers are sensitive to sound (see 4.3.8), clapping in hands or creating any noise helps to find the resonance frequency. Then the cantilever is sensitive to acoustic vibrations and "responds" to the sound. For example the Q-factor can be filtered out of the measurement, which is important for the spring constant k-test (see 4.3.7. The Q value has an great impact on the results for the final spring constant value.

- The ring-down measurement 4.3.4:
  Another way to measure the Q-factor is the ring - down measurement. For this the scope settings have to be set properly, mostly the sampling time should be high. After blocking the Driving arm the oscillations are decreasing, until the cantilever stops moving. Figure 4.13 shows the characteristic ring-down-measurement with amplitudes dropping down to almost zero, when the driving beam is completely blocked.

- The Radiation Pressure test 4.3.6:
  The system under study should be dominated by radiation pressure, the reflectance curve is compared with the deflection curve. For the radiation pressure test the displacement of the cantilever is measured with the Readout arm. The cantilever displaces due to the "kicks" at

Figure 4.9: This figure shows the Imaging arm.

the right frequency of the modulated laser beam and at different wavelengths on the driving arm. The static measurement 4.3.5 is controlled with the Germanium diode simultaneously.

- The spring-constant k test 4.3.7:
  To obtain a quantitative analysis, we checked the spring constant (similar to the idea in [30]) because the reflectance level of the cantilever does not give an information about the actual force which is applied on the cantilever. For this measurement we set the optical chopper to the resonance frequency of the tested cantilever and the DL Pro is tuned to 1064 nm. We dropped the laser power with the tunable attenuators step by step until the laser beam is completely blocked. We recorded the amplitude on the measurement side and the 8% of the split incident as well as the reflected beam.

4.1.4   Imaging

In order to align both laser spots properly we inserted a CCD camera (Point Grey, Chameleon) perpendicular to the translation stage. In front of the CCD, a biconvex lens with a focal length of 75 mm collects all the scattered and transmitted laser lights of the Readout and Driving arm (see figure 4.1.4). Important is to have a convex lens which collects all the light. Between CCD and lens we switch a tunable attenuator, in order not to destroy or over-saturate the camera.

There was no need for an additional light source to make the MOMS structure visible. Via the transmitted driving beam on the chip or with a lens tissue and scattering of the Readout beam on the cantilevers the laser-spots are aligned on the desired cantilever (see figure 4.1.4). With this technique

the micro mechanical structures are nicely visible in the scattered or transmitted light.

4.2 Vacuum

The Q - factor is around 200 000 at 4 K and a pressure around 10^{-5} mbar or 10^{-6} mbar [49].
In air we measured Q - factors up to 10. If the motion is dominated by the pressure of light, then this will be more visible in vacuum. The cantilever could be kicked by the heating of the air around the cantilever. Pumping the air in chamber would remove this effect.
We got two options, the one was to evacuate the whole set - up or just a small jar for the chip. We choose the elegant and second way.

Chamber: For the vacuum tests we applied the same set-up but pumped out the air in the custom made mini - vacuum chamber (shown in figure 4.5). The chamber has a diameter of 1 inch. Depending on the O - rings it has a thickness between 20 mm and 15 mm. This is a modification of the sample holder. The middle part consists of the supporting assembly (diameter one inch) and a fixing part (half inch in diameter) enough to cover the chip and apply a force to keep the cantilever chip in a vertical position in the chamber. The flat head cap screws are used instead the M2 screws because they are smaller and thinner. All the parts are made out of aluminium. This is more advantageous for the required vacuum conditions.
The front part and the back part, both are 1 inch in diameter with a open hole for the 1064 nm - coated Layer Tech laser windows which we glued with vacuum epoxy into the metal part.
The idea is to fix all the parts with metal retaining-rings including

1. the front part with a 1064 nm laser window

2. the first O - ring

3. the middle part with the chip

4. the second O - ring

5. the back part with a 1064 nm laser window

in the same X-, Y- translation stage.
The back piece has a few millimetre long metal tube. It was soldered on the back of the vacuum chamber for the chamber-pump connection. This tube has an outer diameter of 3 mm. The mini custom-made chamber reaches pressures of $\approx 10^{-3}$ mbar.

Windows: The windows are fused silica laser windows from Layer Tech

company with an anti-reflective coating on both sides for the wavelength range between 1030 nm to 1064 nm (when the laser beam shines under 0°). The AR coating prevents multiple-reflections of the beam of the laser beam in the mini vacuum chamber.

Connections: From the metal tube we connect a black plastic tube, which is short for improving the performance of the vacuum. From there, it is connected to a full range (from 1200 bar to 10^{-8} mbar) gauge and a ON/OFF - valve, both from Pfeiffer Vacuum. All this is in between the mini custom-made chamber and the vacuum pump.

Vacuum Units: The turbo pump station (HiCube 80 Eco) has a DN 63 ISO - K with a high vacuum flange. Inside the vacuum stand there is a diaphragm pump (MVP 015-2), a dry compressor vacuum pump and the control units. The lowest, reachable pump pressure is around 10^{-7} mbar.

4.3 Results

The following subsection focuses on the measurement results. The description of the set-up and measurement can be reviewed in the section 4.1.

4.3.1 Measurements

In the ideal case, the displacement of the cantilever is due solely to the momentum transfer imparted by reflecting photons.
In the real case, we will always measure a small amount of heating and, simultaneously, radiation pressure. The point is how good can you improve the system under study, i.e. suppress the heating effect as good as possible but at the same time increase the values for the momentum transfer. See 2.3.1, 4.3.7. A separation of both effects (radiation pressure and heating) is necessary for identifying and understanding the characteristics of both.

4.3.2 Waist Measurements

Figure 4.10 shows the waist at 990 nm and 12 mm away from the middle of the second focusing lens on the Driving arm. The fit through the measured data points is the error function. The fit-function is a error function, which is a defined function in the data-analysis software (Origin). The general form is given as $erf(x) = \frac{2}{\sqrt{\pi}} \int_0^x exp(-t^2)dt$.
This gives for the waist 0. 1794 ±0.0019 mm which is reused for the point with the smallest waist with respect to the position 4.11.
4.11 includes all the four different positions with a fit through the waists of 2.73. The smallest waist with $w_0 = 7.850 \pm 0.013$ μm is positioned 0.41±0.001 mm away from the middle of the lens.

wavelength	waist	error	calc.waist
[nm]	[μm]	[μm]	[μm]
990	7.850	±0.013	7.88
1000	8.480	±0.59	7.96
1010	8.160	±0.59	8.04
1020	8.300	±0.068	8.12
1030	8.080	±0.057	8.20
1040	9.810	±0.063	8.28
1050	8.250	±1.3	8.36
1060	6.720	±0.61	8.44
1070	8.190	±0.52	8.51
1080	9.650	± 0.72	8.59
1090	10.150	±0.25	8.67
1100	7.8008	±0.27	8.75

Table 4.1: This table shows the wavelengths and in the first column, the measured waists with the error. The error results from the fit through the waist. For comparison the last column includes the calculated (expected) waists with 2.65. For w_{01} we took 1 mm.

Table 4.1 is a summary of the waists at different wavelengths. The waist shrinks to ≈ 8 μm to 10 μm from 990 nm to 1100 nm, which is necessary for pointing most of the laser power onto the cantilever head. For the 100 μ m cantilever head at 1064 nm, the power of the transmitted light and the ingoing power was measured to be approximately 2% - 5% of the ingoing laser light. If $\approx$ 10.82 mW directs to the cantilever, then 10.03 mW are hitting the cantilever head. This means more than the 95% of the beam is directed onto the cantilever head.

4.3.3 SPD Sensitivity Measurement

Figure 4.12 is a zoom in the linear range of a SPD, when it is translated from side to side. From the linear regression, $y = Ax + B$, the slope value A is the conversion factor. The maximum value should be equal to the minimum value before the function starts turning. In figure 4.12 the maximum value is 4.4 ±0.004 V and the minimum value is -4.4±0.004 V.
In 4.12 the slope is A = 39703±754 V/mm . This value will be used in the following for the conversion in m for the vacuum tested 1 mm long and 5 μm wide arm length plus 100 μm head cantilever. According to Hooke´s Law, equation 2.1, the laser spot deflection at the SPD will range, for a diode laser that emits max. 10 mW - 15 mW, between $\approx$1 μm and 10 μm which corresponds to tiny motions compared to the linear range of the SPD of 1.5 mm.
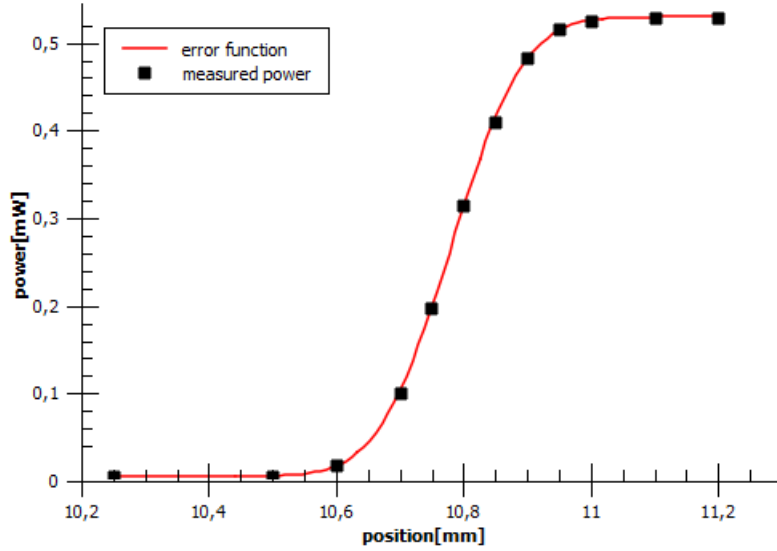
Figure 4.10: Here is one error function plotted. This graph includes one example for the 990 nm waist measurement. See table 4.1 for more details.
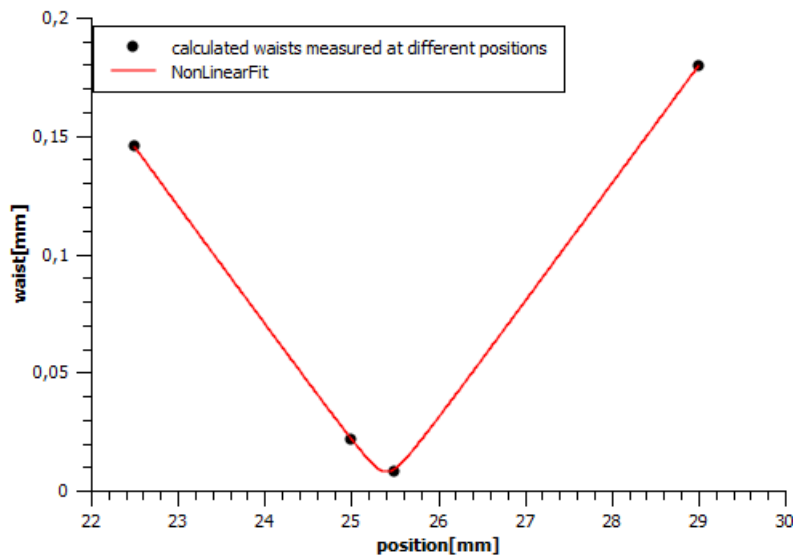

Figure 4.11: After measuring the waist at four positions you can find the position of the smallest waist by fitting with the following function 2.73.
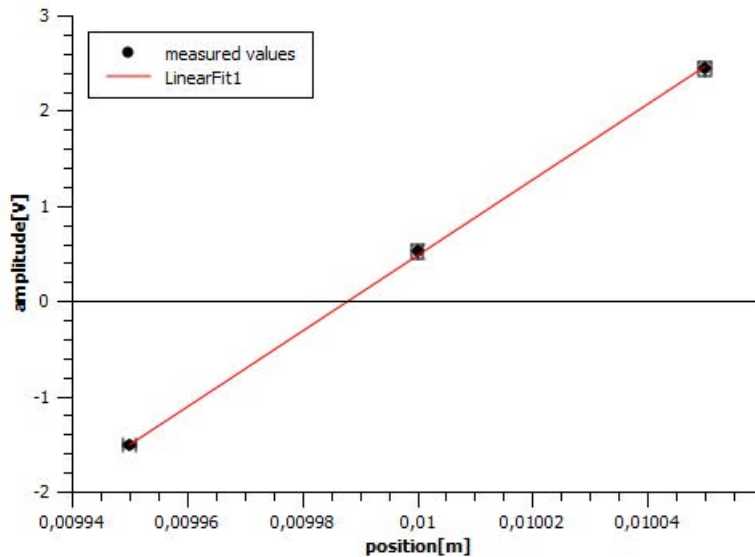
Figure 4.12: This plot shows the sensitivity measurement curve for the 1mm long 5 μm wide and 100 μm cantilever. It has a slope of A $= 39703\ V/mm$, which will be used in the following to convert the motion of the cantilever into a distance. This value will be used even for the k -test 4.3.7

4.3.4 Resonance Curve and Ring Down Measurement

Figure 4.14 shows a typical resonance curve for the 3 mm $- 20\mu$m -100μm cantilever. The Q-factor is defined as π times the time where the amplitude drops over the time $1/e$ times the resonance frequency. This measurement is giving more accurate Q-vales without scanning over the frequency spectrum 4.13.

4.3.5 Static Reflection

Figure 4.15 compares the normalized static reflection with the normalized reflection curve in order to have a direct comparison in figure 4.16.

4.3.6 Radiation Pressure Test

In figure 4.15 the upper graph is the displacement of the cantilever from 994 nm to 1050 nm for the 3 mm long cantilever arm, 20 μm wide cantilever arm and 100 μm cantilever head, tested under ambient pressures. The static reflection (green coloured) measurement matches with the reflectance curve (blue coloured). The red coloured curve is modelled with VERTICAL-software.
Figure 4.16 shows the "reversed" reflectance curve, which we also observed
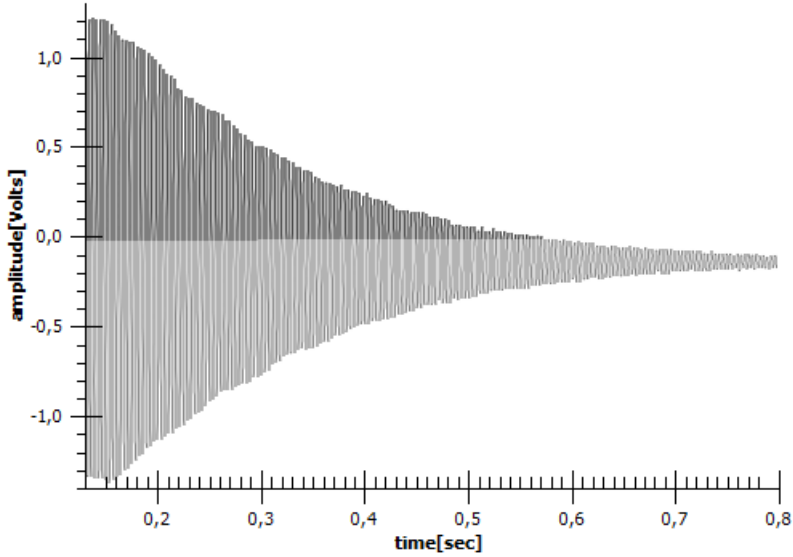
Figure 4.13: This is a ring-down measurement at pressure of $\approx 10^{-3}$ mbar with a Q-value of $\approx$1200. The Q-value is determined with 2.58.

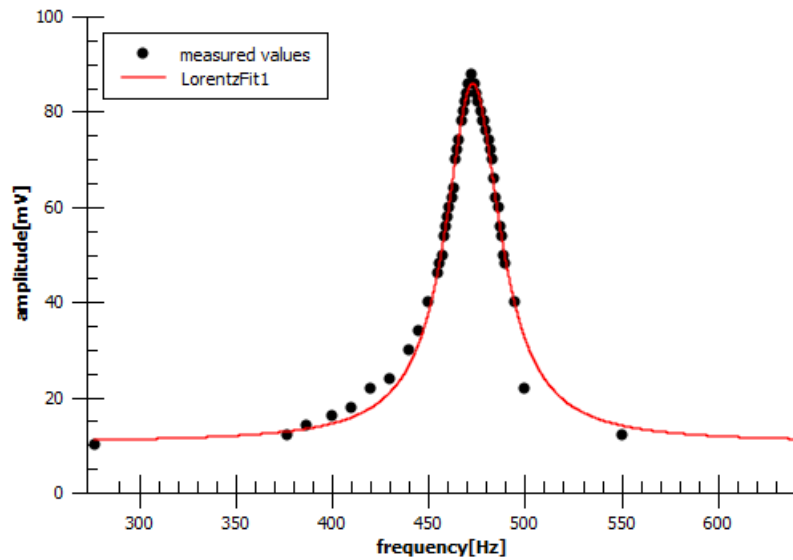

Figure 4.14: From left to right: (left) The ring - down measurement for the 1 mm - 5 μm -100 μm cantilever taken directly from the scope Q- value: 1228 $\pm$101 at 10^{-4} mbar.(right) This curve is made for in air for the 3 mm - 20 μm -100 μm cantilever, with a Q value of 8.52$\pm$0.04
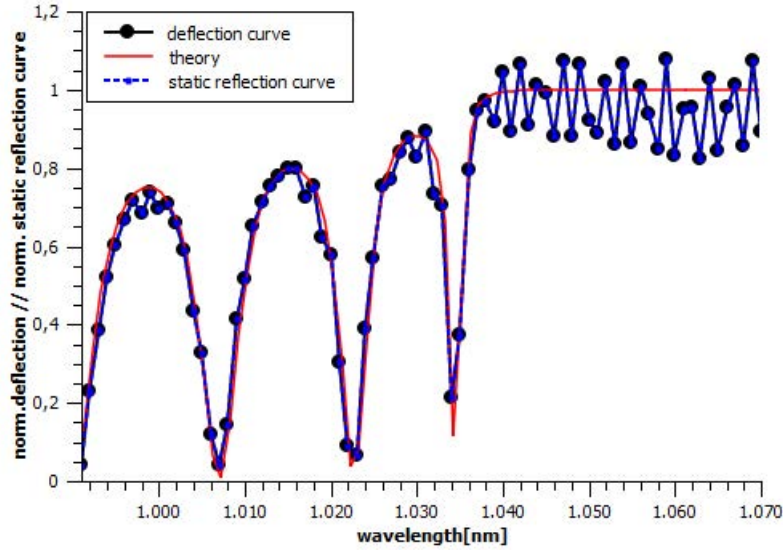
Figure 4.15: This graph includes the theoretical curve which was modulated with VERTICAL on the computer (red curve), the static reflection (blue dotted line) and the response of the mirror material and the deflection curve (black line) for a 3 mm $- 10$ μm $- 100$ μm device at atmospheric pressure.

during our measurements for different sets of cantilevers. A one-side "coated" cantilever shows an unexpected reflectivity curve, most likely due to heating effects caused by dirt or any other additional surface coatings. For this measurement two different cantilevers are tested.

4.3.7 k -Test

In vacuum we measured for the 1 mm long, 5 μm wide and 100 μm head cantilever (the upper graph in 4.18) and for the in air tested 3 mm long, 20 μm wide and 100 μm head cantilever (lower graph in 4.18). The results are summarized in 4.2 and compare the measurement with the numbers from the simulation. For calculating the physical displacement of the measured data, we convert the Volts in meters by using the conversion factor, in V/m, from the sensitivity measurement (4.3.3) and calculate the physical displacement of the cantilever Δx_{dis}

$$\Delta x_{dis} = \frac{\Delta x_{spot} \cdot l_{Canti}}{f} \cdot \frac{1}{2 \cdot Q} \tag{4.1}$$

where Δx_{spot} is the motion of the cantilever converted in meter, l_{Canti} is the length of the cantilever arm, f is the distance (focal length of the lens) between the lens which collimates the light to the SPD and Q is the quality
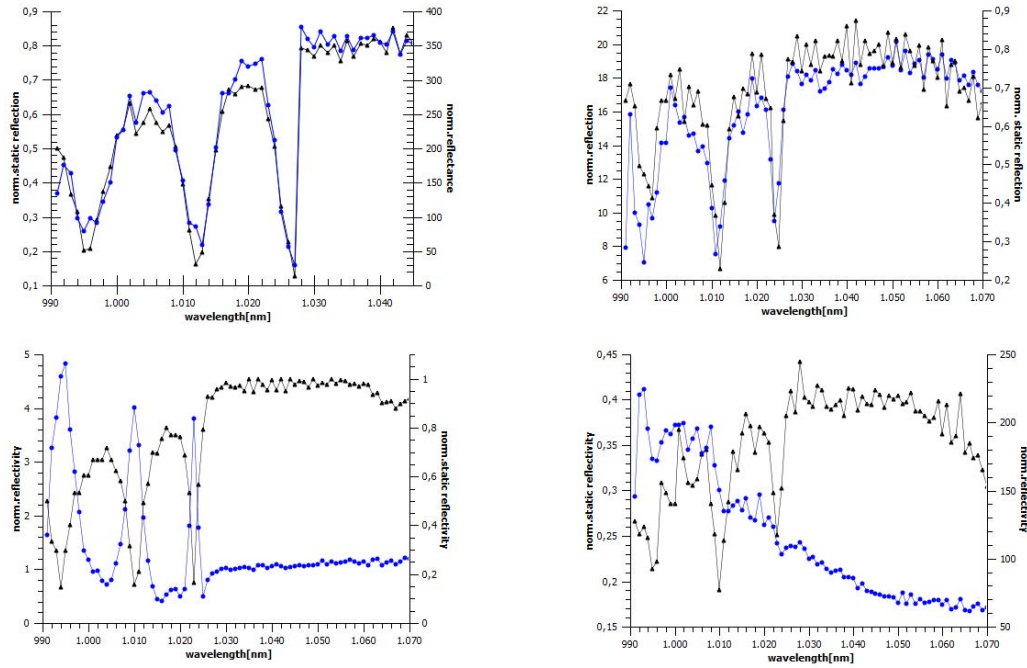
Figure 4.16: The graphics are showing a special case where we explored a different reflectivity curve due to dirt or any additional coating like vacuum grease only on one side of the cantilever. Two different cantilevers are compared: (upper and lower left graphs, blue line with squares - deflection curve and the black line with triangles - static reflection) 5 mm $-$ 5 μm $-$ 100 μm cantilever (upper and lower right graphs) 2 mm $-$ 10 μm $-$ 100 μm cantilever. On the left both measurements are done in vacuum at $\approx 10^{-4}$ mbar. The difference is that the upper reflectance graph perfectly matches with the static measurement but in the lower one, for the 2 mm $-$ 10 μm $-$ 100 μm cantilever the reflectance curve has its extremal points inversed. The measurements are repeated at atmospheric pressures and the chip was turned. The cantilevers are driven on the uncoated side. In the upper-right graph the reflectivity curve matches with the static reflection and (lower-right) for the coated cantilever a different behaviour is observed.
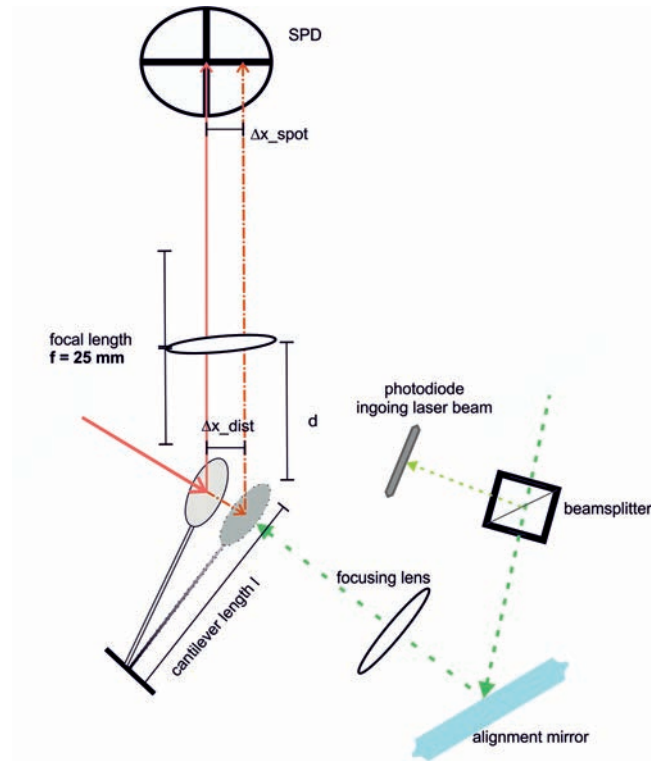
Figure 4.17: Above the k -test is drafted. The red line corresponds to the Readout arm where we employed the optical lever method where light is directed to the cantilever head and reflected off the cantilever. The reflected laser beam goes through a collimating lens (focal length = 25 mm) to the SPD. The physical displacement of the cantilever before the lens (see in the text and in the calculations below) is Δx_{dis} (4.1) and Δx_{spot} corresponds to the displacement of the laser beam. The green dotted line correlates to the Driving arm. The Germanium diode collects the ingoing beam 8% split laser light. The light is point on a mirror surface through a focusing lens (waist depending on the wavelength can be taken from 4.1) and points at the cantilever head.

factor (from 4.3.4). In general, a pendulum swings after "kicking" it constantly with a periodic force twice before it places itself back to the starting position, therefore we inserted a factor of two in the denominator. See 4.3.7. When the cantilever is periodically excited with a 20 mW strong laser light than the force, calculated with 2.74, is 4.2×10^{-10} N. The spring constant value from 4.2 for the 3 mm long,10 μm arm width and 100 μm with the resonance frequency at $\approx$839.6 Hz, is $k_{Comsol} = 0.0011$ N/m. With $l_{Canti} = 0.003$ m for the cantilever arm length, the focal length is set to f = 0.025 m, Q = 10 and for a peak-to-peak value of the periodic function is 0.143V the spot motion Δx_{spot} is 3.6 $\times 10^{-6}$ m. Then the physical displacement of the cantilever, computed with equation 4.1, is $\Delta x_{disp} = 2.2 \times 10^{-8}$ m.

It is important to understand that there is a huge difference between Δx_{spot}, which corresponds to the spot motion of the laser beam at the SPD, and gives the actual or physical displacement Δx_{dis} of a cantilever through a lens.
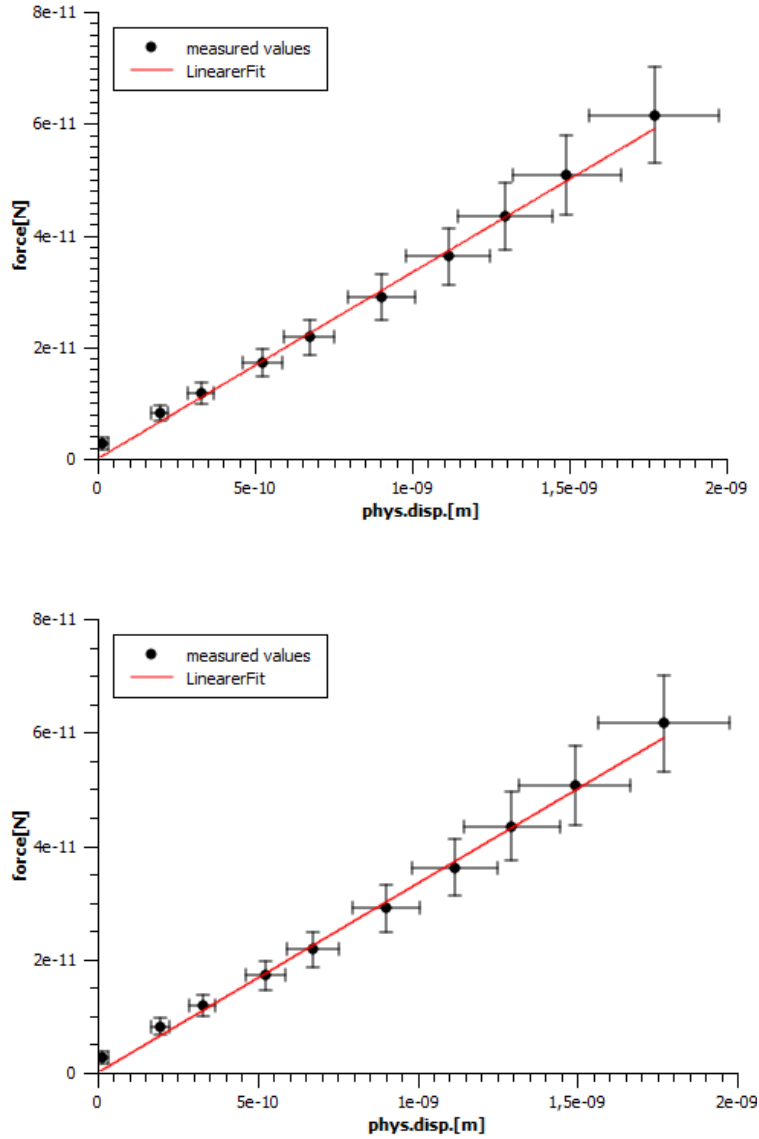
Figure 4.18: From top to bottom: In vacuum (top) the result for the 5 mm
$- 5$ μm $- 100$ μm cantilever the is 0.0333 ± 0.0003 N/m. (bottom) This
measurement is the k-test result for the 3 mm $- 20$ μm $- 100$ μm device.
The measured k value in air is 0.0009 ± 0.00006 N/m. For comparison see
4.2.

AIR	l_c	w_c	d_c	ω_M	ω_C	k_M	k_C	rel.err.	$<x^2>$	Q
	[mm]	[μm]	[μm]	[Hz]	[Hz]	[N/m]	[N/m]	[%]	[m]	
1	3	20	100	471	530.1	0.0009	0.0077	755	7.3×10^{-10}	9 ± 0.3
2	2	10	100	750	839.6	0.0023	0.011	378	6.1×10^{-10}	18 ± 1
3	2	20	100	1002	1014.8	0.0053	0.023	334	4.2×10^{-10}	30 ± 1
4	1.5	10	100	2250	1478.8	0.010	0.032	216	3.5×10^{-10}	50 ± 6
5	1.5	5	100	1003	1129.6	0.019	0.016	16	5.1×10^{-10}	237 ± 181
VACUUM										
1	1	5	100	1888	2141	0.0333	0.0496	49	2.8×10^{-10}	1228 ± 101

Table 4.2: This table compares the measured k values tested in air and in vacuum. The first three columns contain the cantilever arm length l_c, cantilever arm width w_c, and the diameter d_c of the mirror head.(In figure 3.3 the cantilever shape is shown.) The next two columns are comparing the measured frequency ω_M with the COMSOL values ω_C. The next three columns are showing the measured k-value k_M and the COMSOL-values k_C plus the relative error of both. The last row includes the Brownian Motion of the cantilever. This is in truth the minimal motion which the cantilever can do. For calculation this we took $<x^2> = \sqrt{\frac{k_B \cdot T}{k_C}}$, where k_B is the Boltzmann Constant, T is the temperature here 300 K room and k_C is the COMSOL-spring constant.

loudspeaker level	sound level meter	amplitude	error
[%]	[dB]	[mV]	[mV]
100	79.2	315	±9
75	64.7	177	± 35
50	65.9	114	± 12
25	59.4	50	± 2

Table 4.3: Sound level meter results. The higher the loudspeaker the higher the amplitude. This shows that the cantilevers are high sensitive to sound.

4.3.8 Acoustic Test

During the measurements we realized that this system is extremely sensitive in air to the acoustic vibrations. Talking during air measurements was killing the real displacement amplitude. The measured background noise, measured with a noise level meter was during the measurements in the lab 56 dB. In the following table you can read the lowest and highest amplitude of the cantilever when it is driven with a 60 seconds long periodic sound (like a sine or cosine function) at the resonance frequency when we vary the loudspeaker level. In this case the resonance frequency of the tested 3 mm long, 10 μm wide and 100 μm head cantilever is tested at 472 Hz.

The test was to drive the cantilever at the resonance frequency acoustically. The results are shown in table 4.3.7 and in table 4.3.8.

4.3.9 Error Analysis

Propagation of Errors of Precision:
See for this [54]. Often we have two or more measured quantities that we combine arithmetically to get some result. Assume that the two directly measured quantities are X and Y, with errors X and Y respectively. The measurements X and Y must be independent of each other. The error in the result Z is the following one:

$$\Delta Z = Z \sqrt{\left(\frac{\Delta X}{X}\right)^2 + \left(\frac{\Delta Y}{Y}\right)^2} \qquad (4.2)$$

This rule is valid for $Z = X \cdot Y$ or $Z = \frac{X}{Y}$, which we always have in our calculation.
For $Z = X + Y$ and $Z = X - Y$ the error is defined as

$$\Delta Z = \sqrt{\Delta X^2 + \Delta Y^2} \qquad (4.3)$$

If $Z = \bar{b} \cdot X^a$, where $\bar{b}, a$ are arbitrary, fixed constants and when a is equal

sound level meter [dB]	frequency [Hz]	amplitude [mV]	error [mV]
61.7	390	62	±10
65.4	471	90	±22
66.1	472	332	±20
66.9	490	160	±8
69.4	500	102	±10

Table 4.4: Sound level meter results for the same cantilever at different frequencies and loudspeakers set to 100%. Like in the optical driving tests the excitation of the resonance frequency is, even if the loudspeaker is at the highest level, higher than for any arbitrary frequency.

to $a = 1$. The error, for the multiplication of a erroneous quantity with any arbitrary constant, is given as

$$\Delta Z = Z \cdot \frac{\Delta X}{X} \tag{4.4}$$

The percentage of the relative error the following formula is computed with

$$rel.err. = \frac{|\acute{X} - X|}{\acute{X}} \cdot 100 \tag{4.5}$$

where $\acute{X}$ is the measured value and X is the true value.

Errors of the different Quantities:

1. Waist measurements: The errors are from the non-linear fits, which were done in Origin.

2. Sensitivity measurement: We took the for the X-values the smallest increment on the scale of the micrometer screw driver which is $\pm 10 \mu m$, for the Y- values the voltage on the scope differs between $\pm 0.02V$. Both is taken into account in the weighted linear fit. The error which results from the linear fit.

3. Resonance curve: The error for the Q-value results from an Lorentzian fit through the measured data.

4. k - test: The error is propagating in the analysis of the k-test. The list includes the error of the measured values:

   - Distance between cantilever and lens (before SPD): $\pm 0.002m$
   - Cantilever length: $\pm 2 \times 10^{-6} m$
   - Voltage of Germanium diodes: $\pm 0.01V$

- Powermeter: Can be neglected, because the standard deviation (PowerMax-software) drops down to few nW after some time .

- Sensitivity measurement: See above.

- Resonance curve or ring down measurement: See above.

- Scope error: limited to the displayed values on the scope ... $0.04V$ but in general $\pm 3\%$ of the measured value

- Toptica motorized wavelength switch: $\pm 0.2nm$

- Germanium Calibration: The errors we have from the stepper of the diode laser motor and the powermeter which we can neglect because after a certain time the standard deviation drops down to nW

Chapter 5

Conclusion and Outlook

In this section we will sum the main results up and try to give ideas how to extend the experiment.

This experiment is on the one hand a demonstration experiment but also could be used as a new AFM - cantilever calibration method (like in [56, 57, 58, 59] or [60]) based on optical methods. All the others properties, like the mass, spring constant can be derived from the k - test once we improved this measurement (4.3.7).

5.1   Results

1. The Waist Measurement:
   The waist measurement is an essential step for the radiation pressure demonstration. The results of the static measurement and reflectivity curve changed when the spot size was smaller than the cantilever head. Reflections at the Germanium diode and at the SPD were measurable with an higher accuracy.

2. The SPD Sensitivity Measurement :
   A detector with a high resolution, working noiseless at low optical powers, is important for the measurements. The current detector is sensitive and performs the task. Questionable is, if there is an other dection-scheme, which would increase the sensitivity of the measurements.

3. The Resonance Curve and the Ring-down Measurement :
   Initially the resonance curve was used for Q-value estimation but in vacuum the Ring-down measurement gave more accurate numbers and values.

4. The Static Measurement :
The reflectivity of the DBR material with respect to the wavelength was tested (see chapter 3) from Stanford Photothermal Solutions company. The measurement result is shown in figure 3.1. Some of the slopes are not visible.
Whereas, we showed with this easy and cheap experimental set-up, which requires only a Germanium diode, a tunable laser and the tested DBR material, that you can measure precisely accurate.

5. The Radiation Pressure Measurement :
The radiation pressure test was measured after reducing the spot size. This measurement is an indication that the pressure due to light is dominating in our system and that our system is driven by the pressure of light.
In air and in vacuum the measurements match with the static reflection curve, except in the case where the cantilever was coated on only one side. The measured results are showing that the reflectance curve is reproducible. The new behaviour, described in figure 4.16, says that you can extract more information by changing or adding the cantilever surface.

6. The Spring-Constant(k)-test :
This spring-constant test was done to obtain a more quantitative measurement than the radiation pressure test. Significant are the high relative errors, in table 4.2, between the spring constant values k_C form the COMSOL-software and the spring constant values k_m from the measurement.
The longer the cantilever is, the higher is the relative error.
For the analysis of the k-test measurements we used

$$\Delta x_{disp} = \frac{\Delta x_{spot} \cdot l_{Canti}}{d} \qquad (5.1)$$

where Δx_{disp} is the displacement of the cantilever, Δx_{spot} is the displacement of the cantilever measured at the SPD and l_{Canti} is the cantilever length. The quantity d is the distance from the cantilever to the lens, which is, in the ideal case, equal to the focal length of the lens.
The displacement at the at the SPD Δx_{spot} depends only on the ratio of the cantilever length to the SPD distance, without a lens.
Test-measurements showed that displacements at the cantilever Δx_{disp} and displacements at the SPD Δx_{spot} after the lens are different, when the system is analysed with 5.1.
The following formula, which is drafted in figure 5.1, includes the distance from the cantilever to the lens d, the distance between the lens

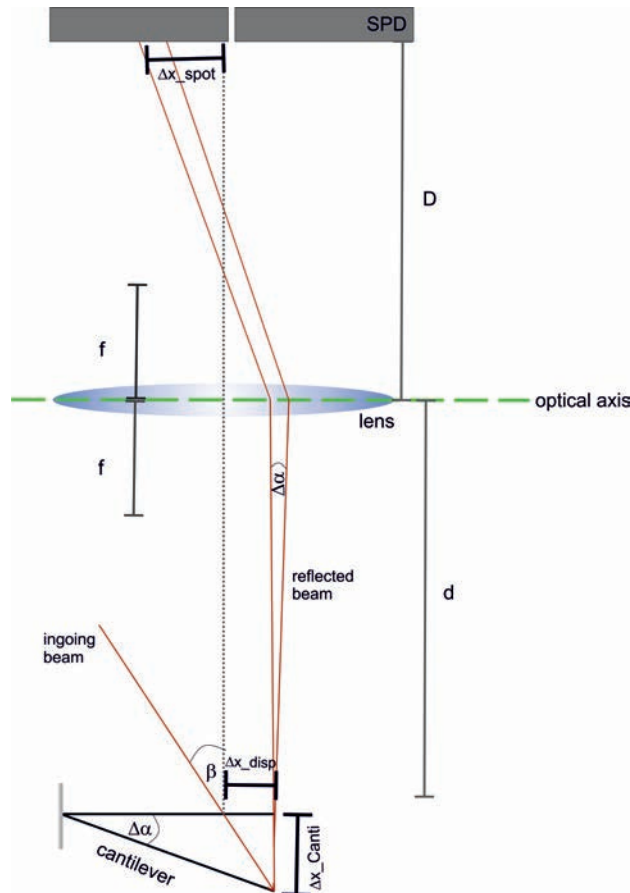Figure 5.1: This figure shows the cantilever-lens configuration in the experimental set-up. The reflected beam has a linear part and an additional angle. Note that $\Delta x_{Canti} = \Delta x_{dist} \cos(\beta)$. When a laser beam shines perpendicular on a reflective surface than the reflected beam is always shifted under an angle $\Delta \alpha$, which is drawn in the figure between the two red lines.

to the SPD D, the focal length f and the ingoing-angle β as well as the turning angle $\Delta\alpha$. With the matrix method (2.2.1) we find

$$\begin{bmatrix} 1 & D \\ 0 & 1 \end{bmatrix} \begin{bmatrix} 1 & 0 \\ \frac{-1}{f} & 1 \end{bmatrix} \begin{bmatrix} 1 & d \\ 0 & 1 \end{bmatrix} \begin{bmatrix} \Delta x_{disp} \\ \Delta\alpha \end{bmatrix} = \begin{bmatrix} \Delta x_{spot} \\ \Delta\bar{\alpha} \end{bmatrix} \tag{5.2}$$

and can write for the spot motion

$$\Delta x_{disp} = \frac{\Delta\alpha L^*}{\cos\beta} \tag{5.3}$$

and for the cantilever displacement we have

$$\Delta x_{Canti} = \Delta x_{dist} \cos(\beta) \tag{5.4}$$

With equation 5.3 for 5.2 we find

$$\begin{bmatrix} 1 & D \\ 0 & 1 \end{bmatrix} \begin{bmatrix} 1 & 0 \\ \frac{-1}{f} & 1 \end{bmatrix} \begin{bmatrix} 1 & d \\ 0 & 1 \end{bmatrix} \begin{bmatrix} \frac{\Delta\alpha L^*}{\cos\beta} \\ \Delta\alpha \end{bmatrix} = \begin{bmatrix} \Delta x_{spot} \\ \Delta\bar{\alpha} \end{bmatrix} \tag{5.5}$$

In the following we are interested only in Δx_{spot} the spot displacement. Then Δx_{spot} is given as

$$\Delta x_{spot} = \left(D + d\left(1 - \frac{D}{f}\right) \right) + \left(\frac{\left(1 - \frac{D}{f}\right) L^* \Delta x}{\cos\beta} \right) \tag{5.6}$$

If the ingoing beam comes under an angle $0 < \beta < 45°$ then the second terms has to be modified with the factor $F = 2\sin^2\beta$

$$\Delta x_{spot} = \left(D + d\left(1 - \frac{D}{f}\right) \right) + \left(2\sin^2\beta \frac{\left(1 - \frac{D}{f}\right) L^* \Delta x}{\cos\beta} \right) \tag{5.7}$$

We assumed for the cantilever displacements that the cantilever beam is fixed.
The cantilevers used here, have a very low spring constant, due to this properties an additional bending of the cantilever tip can appear.
For a increasing cantilever deflection and/or angle of loading the non-linear behaviour of the cantilever will be discussed.
In our measurements the cantilevers ([9]) are bend by a point force $|\vec{F}| = F$ in the z-direction with a force $|\vec{F}| = F$. This corresponds to the optical power of our laser, which is directed to the cantilever head. $z(x)$ corresponds to the distance from the unloaded position of the cantilever to the tip deflection point along the the x-axis, which is shown in figure 5.2. This is given as

$$z(x) = \frac{1}{2} \frac{Fl}{EI} \left(x^2 - \frac{1}{3l} x^3 \right) \tag{5.8}$$
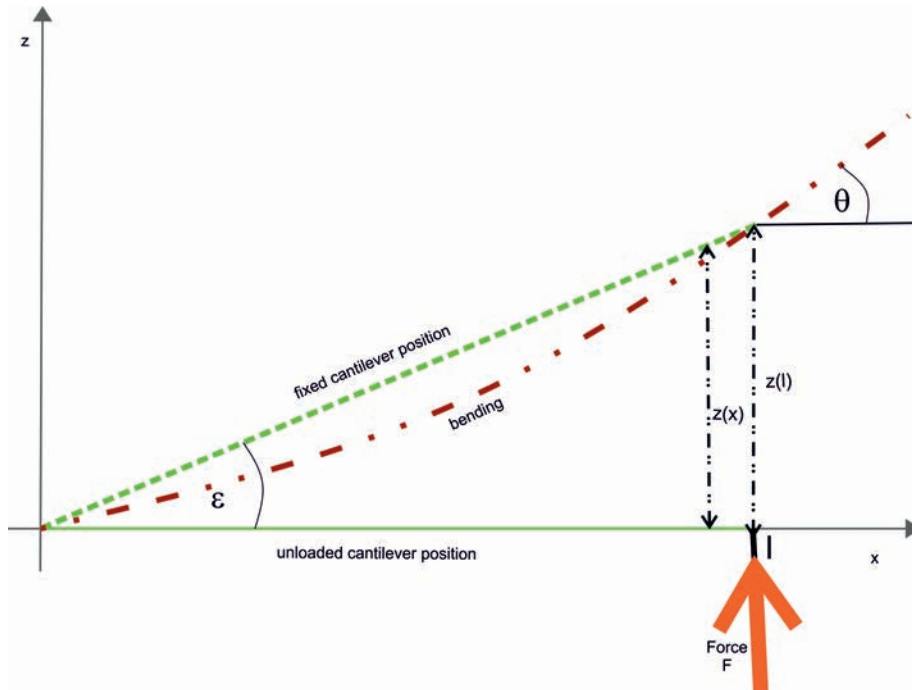
Figure 5.2: This figure shows an unloaded cantilever (marked in green) with the length l in the x-z plane. It shows two possible cantilever deformations when a point force F is applied on the cantilever. The red dotted line shows a bending cantilever. The angle ϵ is the angle between the unloaded and the fixed cantilever position (dotted green line). The tip angle is θ (see equation 5.13). $z(x)$ corresponds to the distance from the unloaded position of the cantilever to the tip deflection point along the the x-axis. The deflection at tip is here $\Delta x_{disp}(l) = z(l)$. This figure shows that the expected tip deflection is, for a bending cantilever, is bigger compared to a cantilever, which displaces linear and stiff from the unloaded position.

where l is the cantilever length, E is the Young´s modulus and I is the moment of inertia. Whereas, the deflection at tip is

$$\Delta x_{disp}(l) = z(l) = \frac{1}{3}\frac{F}{EI}l^3 \tag{5.9}$$

The spring constant is defined as

$$k = 3\frac{EI}{l^3} \tag{5.10}$$

and connected to the $\Delta x_{disp}(l)$ and F with the Hooke´s Law 2.1. The angle, in the x-z plane at the tip gives the laser beam deflection is

$$\theta = \dot{z}(l) \tag{5.11}$$

The tip deflection is then

$$\dot{z}(l) = \frac{1}{2}\frac{F}{EI}l^2 = \frac{3}{2}\frac{z(l)}{l} \tag{5.12}$$

For the relation between the tip deflection angle and the tip deflection distance we find

$$\theta = \frac{3}{2}\frac{\Delta x_{disp}}{l} \tag{5.13}$$

This result shows that the expected tip deflection, when cantilever is bending, is a factor $\frac{3}{2}$ times bigger compared to a cantilever, which displaces linear and stiff from the unloaded position.

Additionally, the usual detection base of the cantilever is in the x-z plane $\theta = \theta(x, z)$ and the displacements are detected with the right-left configuration of the SPD. For millimeter long, low spring-constant cantilevers torsional effects can occur and the cantilever tip can twist. Since the tip angle is defined as 5.13, the Hooke´s Law 2.1 the angular spring constant is

$$F = k_{twist}\theta \tag{5.14}$$

and the relation between the spring constant, when $k = \frac{1}{4}Y\frac{wt^3}{l^3}$, is

$$k_{twist} = \frac{2}{3}kl \tag{5.15}$$

We measured the spring-constant only for the first out-of-plane mode, interesting is if the second higher mode gives the same result.

Besides, for the data analysis we used the values from the Germanium diode, which measures the optical power of the incident beam. Whereas Germanium diode two records the reflected beam with the laser beam losses. This should give more accurate information about the driving force.

5.2 Improvements

- Vacuum Chamber:
  We found a elegant way to isolate the cantilevers from its surrounding with the one inch mini - chamber. Measurements in air are good but putting them into vacuum for pressures around $10^{-2}mbar$ the Q increases. Currently you can have pressures around 10^{-3} mbar, which is good but compared to the pressure which Peter Lebedew [26] had in 1901 is this not the optimal pressure. In the the above cited article he claims a pressure of 10^{-7} mbar. In fact this value is quite amazing when you think of the limitations he had to face at that time. Instead Nichols and Hull [27] reached a pressure around 10^{-4} mbar, which is today not so difficult to reach.

- Cantilever Sensor:
  As we saw those structures are really good sound sensors (4.3.8) and lab noise is even lowered by isolating the chip nicely from the surrounding.

- Interferometry:
  The question if a Michelson interferometer or the optical lever arrangement is better for the readout is questionable. The main advantage is that the interferometric configuration will even work for optical powers around $\approx \mu W$ range. See [55].

- Cantilever Characterization:
  This scheme can easily upgraded to full automated system by implementing piezo construction which is moving the laser beam automatically to the center of the SPD and change the position of one of the alignment mirrors stepwise for testing the sensitivity of the detector. For measuring the resonance curve the optical chopper can be modulated via computer control and the amplitude readout from the scope. The Radiation Pressure Test is already running completely automatically. For the k - measurement a motorized attenuator can be used to lower constantly the power of the DL Pro laser.
  Heating effects can be studied by laying on different coatings.

5.3 Conclusion

In conclusion, we showed that the reflectance curve of the MOMS sample, static and dynamic, with respect to the wavelength perfectly matches with the theoretical curve (see figure 4.15). For quantitative analysis, k-test, more investigations are needed (see table 4.2). The calculation from above shows that the relative error should be reduced with new formula 2.39, the cantilever bending formula 5.13 and the twisting formula 5.15.

5.4   Possible Extensions

In 2008 Karrai et.al. said that cooling works in principle for photonic crystals such as a DBR. Cooling requires a micro-mirror which is mathematically described as a harmonic oscillator and mechanical dissipation without fluctuations implies cooling. The difference between the DBR cooling and the cavity cooling schemes is that in the last case velocity dependent force is amplified through the long photon storage time.
In this article [32] the velocity depended force is created by the Doppler cooling of the photons.
This is a very challenging idea but for our current cantilevers, we found out that cooling or heating is not possible. The design of the cantilevers has to be changed. The mass is, for example, too high and the reflectance slope $\frac{dR}{d\lambda}$ has to be steeper.
Doppler cooling would work for cantilevers with a mass of 2.3×10^{-10}kg, a Q-value of 3×10^5 with a frequency of 265Hz and $\frac{dR}{d\lambda} = -5 \times 10^{10}$ at 0.5W optical laser power. If we start from $\approx$ 4K we can cool down to 0.95K.
Problematic are the high powers, which can destroy the DBR material and the the modelling of the $\frac{dR}{d\lambda}$ slope.
Recently, Horsley et.al. [67] claim that the cooling efficiency is for optically trapped rubidium atoms has to be 3 orders of magnitude higher than for photonic crystals such as a DBR. They say that their results can be applied equally well to any system exhibiting a photonic band gap on the same frequency scale.
According to their calculations for a specific pulsed regime, damping remains observable without destroying the system.
The micro machined object are even utilized from the Optomechanics for the second end mirror to entangle the cantilever with the light field [61], or to cool the mechanics down to the quantum ground state .
New experiments are showing that magnetic cantilevers can be used for developing quantum transducers for the quantum computer, cantilevers can be coupled to atoms [62] to have deeper insight into quantum physics. You can produce entanglement of nano - cantilevers by using two of them and putting a BEC in between (see [63]) or the investigation of a nano-mechanical oscillator in the quantum regime with electric dipoles [64]. Creating entanglement of a tunneling spin with mechanical modes of a torisional resonator is theoretically calculated recently [69].
Cantilevers can be used for force sensing, bio -sensors and even for chemical reactions [68] Cantilever can be used as gas flow sensors for flow rate and direction detection ([65]. In any application where you want to measure a force, power - change. Than it is useful for the measurement of masses - as well as single molecule detection.
Kapitulnik et .al. are requiring cantilevers for measuring the fundamental gravity constant [66].

In [70] arrays of cantilevers, with a magnetic tip, are coupled to single spins (NV-centers in diamond) to achieve controlled interactions over distances larger than tens of nanometres. This would pave the way for new exciting experiments in quantum information.

Bibliography

[1] J. Kepler, *De Cometis Libelli Tres Augsburg*,1619

[2] O. Romero-Isart, M. L Juan, R. Quidant and J. I. Cirac *Toward quantum superposition of living organisms*, New Journal of Physics, 12, 2010

[3] D.E. Chang, C.A.Regal, S.B.Papp, D.J. Wilson, J.Ye, O.Painter, H. J. Kimble and P. Zoller, *Cavity opto-meachanics using an optically levitated nanoshpere*, PNAS, Vol.107, No.3, 2010

[4] P.F. Baker and M.N. Shneider *Cavitiy cooling of an optically trapped nanoparticle*, Phys. Rev.Lett. A, 81, 023826, 2010

[5] Z. Yin, T. Li and M.Feng *Three - dimensional cooling and detection of a nanoshpere with a single cavity*, Phys. Rev. Lett. A, 83, 013816, 2011

[6] T. Li, S. Kheifets and M. Raizen*Milikalvin cooling of an optically trapped microsphere in vacuum*, Nature Physics, 7, 2011

[7] M. R. Vanner, I. Pikovski, M. S. Kim, C. Brukner, K. Hammerer, G. J. Milburn, M. Aspelmeyer *Pulsed Quantum Optomechanics*, PNAS 15, 1-6, 2011

[8] T. Corbitt, N. Mavalvala *Quantum noise in gravitational - wave interferometers*, J. Opt. B: Quantum Semiclass. Opt., 6, 2004

[9] T. Belendez, C. Neipp, A. Belendez, *Large and small deflections of a cantilever beam*, European Jornal of Physics, Vol.23, No.3, 2002

[10] C. M. Caves, K. S. Thorne, R. W. P. Drever, V. D. Sandberg, and M. Zimmermann, *On the measurement of a weak classical force coupled to a quantummechanical oscillator. I. Issues of principle*, Rev. Mod. Phys. 52, 341, 1980

[11] V. Braginsky and F. Khalili, *Quantum Measurements* Cambridge University Press, 1995

[12] P.-F. Cohadon, A. Heidmann, and M. Pinard *Cooling of a Mirror by Radiation Pressure*, Phys. Rev. Lett.,83, 3174, 1999

[13] A. Ashkin,*Acceleration and Trapping of Particles by Radiation Pressure.*, Phys. Rev. Lett. 24, 1970

[14] S. Gröblacher, K. Hammerer, M. R. Vanner and M. Aspelmeyer,*Observation of strong coupling between a micromechanical resonator and an optical cavity field*,Nature 460, 724-727 (2009)

[15] B. Carazza and H. Kragh, *Adolfo Bartoli and the Problem of Radiant Heat*, Ann. of Sci., Vol. 46, 2, 1989

[16] A. Bartoli, *Il calorico raggiante e il secondo principio di termodynamica*, Nuovo Cimento, 15, 1884

[17] A. Bartoli, *Dimostrazione elementare di un teorema relativo alla theoria del raggimento dato dal Prof. Clausius*, Nuovo Cimento, 6, 1879

[18] J. C. Maxwell, *A Dynamical Theory of the Electromagnetic Field*, Royal Society Transactions, Vol. CLV, 1865

[19] J.J. Thompson, *Elements of the Mathematical Theory of Electricity and Magnetism*, Cambridge, 1895, pp. 420-2

[20] B. Galitzine, *Über Strahlende Energie*, Ann. d. Phys., Vol.47, 1892

[21] Ludwig Boltzmann, *Über eine von Hrn. Bartoli entdeckte Beziehung der Wärmestrahlung zum zweiten Hauptsatze*, Ann. d. Phys., 22, 1884

[22] Albert Einstein, *Über einen die Erzeugung und Verwandlung des Lichtes betreffenden heuristischen Gesichtspunkt*, Annalen der Physik. 322, 6, 1905

[23] S. Gröblacher, J. B. Hertzberg, M. R. Vanner, S. Gigan, K. C. Schwab, and M. Aspelmeyer, *Demonstration of an ultracold micro-optomechanical oscillator in a cryogenic cavity*, Nature Phys. 5, 485, 2009

[24] S. Gigan, H. R. Böhm, M. Paternostro, F. Blaser, G. Langer, J. B. Hertzberg,K. C. Schwab, D. Bäuerle, M. Aspelmeyer, and A. Zeilinger,*Self- cooling of a micromirror by radiation pressure*, Nature 444, 67, 2006

[25] T. Kippenberg, H. Rokhsari, T. Carmon, A. Scherer, and K. Vahala, *Analysis of Radiation-Pressure Induced Mechanical Oscillation of an Optical Microcavity*, Phys. Rev. Lett. 95, 033901, 2005

[26] P. N. Lebedew, *Untersuchungen über die Druckkräfte des Lichtes*, Ann. d. Phy. 6, 1901

[27] E. F. Nichols, G. F. Hull,*Über Strahlungsdruck*, Ann. d. Phy.,12, 1903

[28] O. Frisch, *Experimenteller Nachweis des Einsteinschen Strahlungsrück-stoßes*, Z. Phy. B86, 42 ,1933

[29] R.A.Beth, *Mechanical detection and angular momentum of light*, Phys. Rev. 50,115,1936

[30] D.M.Weld, A.Kapitulnik,*Feedback control and characterization of a microcantilever using optical radiation pressure*, App. Phy.Lett., 89 164102, 2006

[31] H. J. Butt et. al., *Force Measurements with the atomic force microscope: Technique, interpretation and application*,Surf. Sci. Rep., 59, 2005

[32] K. Karrai, I. Favero, C. Metzger, *Doppler Optomechanics of a Photonic Crystal*, Phys. Rev. Lett., 100, 240801, 2008

[33] W. Demtröder, *Experimentalphysik 1: Mechanik und Wärme*,ISBN 3-540-26034-x, 4. Auflage, Springer, 2006

[34] E.Hecht, *Optik*, ISBN 9783486273595, 4. Ausgabe, Oldenbourg Wissenschaftsverlag, 2005

[35] W.Greiner, *Klassische Mechanik 1 :Kinematik und Dynamik der Punktteilchen, Relativität*,ISBN 978-3-8171-1815-1 , 8., überarbeitete Auflage,harri-deutsch Verlag, 2008

[36] Wolfgang Nolting,*Grundkurs Theoretische Physik 2: Analytische Mechanik*,ISBN 3642129498,8. Auflage, Springer, 2010

[37] Landau, L.D. and Lifschitz, E.M. and Ziesche, P.,*Lehrbuch der theoretischen Physik: Mechanik*,ISBN 9783817113262,14. Auflage, harri-deutsch Verlag,1997

[38] B. E. A. Saleh,M.C. Teich,*Grundlagen der Photonik*,ISBN 978-3-527-40677-7,2.vollständig überarbeitete und erweiterte Auflage, Wiley - Vch, 2008

[39] With M. Aspelmeyer *private communications*, 29.June. 2009

[40] Dubravko I. Babic and Scott W. Corzine, *Analytic Expressions for the Reflection Delay,Penetration Depth, and Absorptance of Quarter-Wave Dielectric Mirrors*,IEEE Journal of Quantum Electronics, Vol. 28 No. 2., 1992

[41] G. D. Cole, *MEMS-tunable vertical-cavity SOAs*,PhD - Thesis, Department of Materials, University of California, Santa Barbara, October 2005.

[42] PR Photonics Consulting GmbH, Encyclopaedia of Laser Physics and Technology, http://www.rp-photonics.com/encyclopedia.html

[43] A. A. Tseng, *Nanofabrication: fundamentals and applications*, ISBN 9812705422, World Scientific, 2008

[44] F. Blaser, *Mechanical FEM Analysis and Optical Properties of micromirrors for radiation-pressure experiments*,Diploma Thesis, Universität Wien, 2008

[45] S. Gröblacher,*Quantum opto-mechanics with micromirrors:combining nano-mechanics with quantum optics*, PhD - Thesis, Universität Wien, 2010

[46] G. M. Rebeiz,*RF MEMS: theory, design, and technology*, ISBN 0471201693, John Wiley and Sons, 2003

[47] Thorlabs Tutorial

[48] S.Singh, *All-Optical Optomechanics: An Optical Spring Mirror*, Phys. Rev. Lett. 105, 213602, 2010

[49] These values were measured by Shannon Sankar / Thomas Corbitt, MIT

[50] B. Bhushan, H. Fuchs, *Applied scanning probe methods IV: industrial applications Nanoscience and technology*, ISBN 3540269126,Birkhäuser Verlag, 2006

[51] A. Zeilinger et. al.,*Happy centenary, photon* Nature 433, 2005

[52] Force spectroscopy with a large dynamic range using small cantilevers and an array detector; T.E.Schäffer, J. Appl. Phys., Volume 91, No. 7,2002

[53] G.D.Cole, S.Gröblacher, K.Gugler, S.Gigan, M.Aspelmeyer, *Microcyrstalline $Al_xGa_{1-x}As$ heterostructure for high -reflectivity high -Q micro mechanical resonators in the megahertz regime*, Appl. Phys. Lett. 92, 261108, 2008

[54] J. R. Taylor, *An introduction to error analysis: the study of uncertainties in physical measurements*,ISBN 093570275X, University Science Books, 1997

[55] J.Greve et. al. *A detailed analysis of the optical beam deflection technique for use in atomic force microscopy*, J. Appl. Phys. 72 (I), 1 July 1992

[56] J. P. Cleveland, S. Manne, D. Bocek, P. K. Hansma, *A nondestructive method for determining the spring constant of cantilevers for scanning force microscopy*, Rev. Sci. Instrum. 64 (2), February 1993

[57] J. E. Sader, I. Larson and P. Mulvaney, L. R. White, *Method for the calibration of atomic force microscope cantilevers*, Rev. Sci.Instr. 66 (7), July 1995

[58] E. D. Langlois, G. A. Shaw, J. A. Kramar, and J. R. Pratt, D. C. Hurley *Spring constant calibration of atomic force microscopy cantilevers with a piezosensor transfer standard*,Rev. Sci.Instrum. 78, 093705, 2007

[59] E.J. L. Hutter and J. Bechhoefer, *Calibration of atomic-force microscope tips*,Rev. Sci. Instrum. 64 (7), July 1993

[60] N. A. Burnham et. al., *Comparison of calibration methods for atomic-force microscopy cantilevers*,Nanotechnology 14 ,2003, 1-6

[61] M. Aspelmeyer, S. Gröblacher, K. Hammerer, and N. Kiesel,*Quantum optomechanics - throwing a glance*, J. Opt. Soc. Am. B, Vol. 27, No. 6, 2010

[62] D. Hunger, S. Camerer, T. W. Hänsch, D. König, J. P. Kotthaus, J. Reichel, and P. Treutlein, *Resonant Coupling of a Bose-Einstein Condensate to a Micromechanical Oscillator*, Phys. Rev. Lett. 104, 143002, 2010

[63] C. Joshi et. al., *Quantum entanglement of nanocantilevers*,Phys. Rev. A 82, 043846, 2010

[64] S.Singh et al., *Coupling nanomechanical cantilevers to dipolar molecules*,Phys. Rev. Lett. 101, 263603, 2008

[65] Wang et al., *A Microcantilever - based Gas Flow Sensor for Flow Rate and Direction Detection* ,Microsyst. Technol., Volume 15, Number 8, 2009

[66] J. Chiaverini, S. J. Smullin, A. A. Geraci, D. M. Weld, and A. Kapitulnik , *New Experimental Constraints on Non-Newtonian Forces below* $100\mu m$,Phys. Rev. Lett. 90, 151101, 2003

[67] S.A.R. Horsley, M.Artoni and G.C. La Rocca, *Radiation Damping in Atomic Photonic Crystals*, Phys. Rev. Lett., 107, 043602, 2011

[68] J.L. Arlett, E.B. Myers and M.L. Roukes, *Comparative advantages of mechanical biosensors*, Nature Nanotechnology, Vol. 6, 2011

[69] D.A. Garanin and E.M. Chudnovsky, *Quantum entanglement of a Tunnelling Spin with Mechanical Modes of a Torsional Resonator*, Phys. Rev. X, 1, 011005, 2011

[70] P. Rabl et. al. , *A quantum spin transducer based on nanoelectrome- chanical resonator arrays*,Nature Physics, Vol 6, 2010

[71] Jasper van Wenzel and Tjerk H. Osterkamp, *Quantum Mechanics meets General Relativity in Nanoscale Experiments*, arXiv:0912.3675v2

Acknowledgment

THANKS to my family! You all are so great! Thanks for the support!

THANKS to my FRIENDS! Special thanks to Hatice, Theresa, Julia.

THANKS to Prof. M. Aspelmeyer for giving me the chance to work alone on my project, which I designed by myself, just thanks for the great support and your open ears when I came up with my problems. I am sure that there not much diploma students, who can talk big like me: "Ey, I have my own setup with my own experiment ...and you?" This was somehow good for my "growth" and it was definitely your *Ready for the next level?* - question motivated me in the beginning. No matter what I am writing here or how long I am think about the chance I had - I would not be able to express this in words but ...if there would something like a prize for coolness - you would be the winner!

THANKS to Prof. R. Bertlmann! (Good advices....these are rarer than rubies, gell!?)

THANKS to Roland Blach for building all the small holders, the chamber, parts,.... and Michi Cirkovitsch for the technical support, like the sound level meter,.... and my

THANKS to Alexey, Uros and Florian, Nikolai and Alex.

Curriculum Vitae

Dilek DEMIR

Department of Physics
University of Vienna
Boltzmanngasse 5
Vienna, Austria
E-mail: dilek.demir@univie.ac.at

Gender: female
Date of birth: 16.06.1988
Nationality: Austrian
Place of birth: Vienna, Austria

EDUCATION:

Diploma in Physics
University of Vienna, (2010-2011)
Adviser: Markus Aspelmeyer

Studies in Physics
University Vienna (2006-2010)

POSTERS:

"A table-top demonstration of radiation pressure" at the Frühjahrsmeeting der DPG 2011, Dresden, Germany (March, 2011).

"A table-top demonstration of radiation pressure" SFB meeting 2011, Innsbruck, Austria (February, 2011)

PUBLICATION:

D.Demir, G.D.Cole, M.Aspelmeyer, 2011 (in preparation)

EMPLOYMENT:

Research Assistent, Aspelmeyer Group, QOM - Project (2010)

Working Experience, Aspelmeyer Group about Micromechanical Oscillators (07. 2009)

Exercise Instructor, for the "Übungen zu Einführung in die Physik I (StEOP 1)", University of Vienna, Vienna, Austria, will teach a group of 42 students (09.2011-02.2012)

Teaching Assistant, for the "Frauentutorium", University of Vienna, Vienna, Austria, taught with a second tutor a group of 6-12 students (10.2010-01.2011)

Teaching Assistant, for the Lecture "Einführung in die Physik 2 ", University of Vienna, Vienna, Austria, supporting PC-work, Physik - Wiki (03.2010-07.2010)

Learn Assistant, Learn Assistant in Math and Physics, Lernzentrum, 1120 Vienna, Otto Bondy Platz 2, taught 1-10 undergraduate pupils and graduate students (2009-2011)

OUTREACH:

Open Physics at the Faculty of Physics, Vienna (02.2011)

Einstein Slam jDPG event, Dresden (03.2011)

SKILLS:

Languages German (Bilingual, Native fluency), Turkish (Bilingual, Native fluency), English (Good fluency), Italian (Beginner)

COMPETENCES:

Mentored Programs Participant of the *Frauen Mentoring for female Diploma/PhD students* program at the Faculty of Physics, University of Vienna, Vienna, Austria (2009-2011)

External Participant Support of the University of Innsbruck, Tirol, Austria for the *Introductory Course on Ultra cold Quantum Gases* as an external participant (07.2008)

High School Activity Participant of the *Österreichische Chemie Olympiade* (04.2006)